

IDENTIFICATION OF NEURAL ACTIVITY IN *APLYSIA* ABDOMINAL GANGLIA USING
IMPEDANCE MEASUREMENT

By

HANY ELMARIAH

A THESIS PRESENTED TO THE GRADUATE SCHOOL
OF THE UNIVERSITY OF FLORIDA IN PARTIAL FULFILLMENT
OF THE REQUIREMENTS FOR THE DEGREE OF
MASTER OF SCIENCE

UNIVERSITY OF FLORIDA

2007

© 2007 Hany Elmariah

To my parents and to Sammy and Sarina, whose love and support
has carried me throughout my life.

ACKNOWLEDGMENTS

I thank Dr. Thomas DeMarse and Dr. Rosalind Sadleir, whose direction and guidance were invaluable to the completion of this project and my personal development as a researcher. I also acknowledge Karl Dockendorf, Michael Furman, and Il Park, all of whom made contributions to the experiments described in my work. Finally, I thank April-Lane Derfinyak, who has worked tirelessly to keep every student in our department on track to accomplish our goals.

TABLE OF CONTENTS

	<u>page</u>
ACKNOWLEDGMENTS	4
LIST OF TABLES	7
LIST OF FIGURES	8
ABSTRACT	10
CHAPTER	
1 INTRODUCTION	12
Methods for Studying Electrophysiology of Multiple Neurons	13
Impedance Tomography	18
Ion Channels and Neuronal Impedance.....	18
Experimental Goals.....	20
2 MATERIALS AND METHODS.....	25
<i>Aplysia</i> Preparation	25
Microelectrode Array Setup	26
Data Acquisition	28
Data Analysis.....	31
Least-Mean-Square Adaptive Filter.....	31
Spike Detection.....	33
Moving Average Algorithm	33
3 RESULTS.....	40
Patterns of Activity	40
Applied Currents.....	42
Total Spikes Over Time	43
Moving Average Filter.....	44
Correlating Activity and Resistance.....	45
Frequency Analysis.....	47
4 DISCUSSION.....	64
Patterns of Activity and Raster Plots	64
Applied Currents.....	65
Resistance Changes and Activity.....	66
Microelectrode Arrays and Future Work	71
Functional Magnetic Resonance Electrical Impedance Tomography.....	73

5	CONCLUSION.....	79
	LIST OF REFERENCES	80
	BIOGRAPHICAL SKETCH.....	86

LIST OF TABLES

<u>Table</u>		<u>page</u>
1-1	Summary of firing patterns observed for three primary cell groups on the dorsal surface of the abdominal ganglion	24

LIST OF FIGURES

<u>Figure</u>	<u>page</u>
1-1 Image of a standard microelectrode array from Multichannel Systems	23
1-2 Diagram of the dorsal surface of the abdominal ganglion.....	24
2-1 Multichannel Systems 3-D microelectrode array.....	35
2-2 <i>Aplysia</i> ganglion centered on the dish of a microelectrode array	36
2-3 Oscilloscope function of MEABench on Mac OS X	37
2-4 Spontaneous action potential recorded from abdominal ganglion cell.....	37
2-5 Schematic of the MEA setup.....	38
2-6 Flow diagram of the experimental apparatus.....	38
2-7 Example of LMS filtration.....	39
3-1 Raster plots for spontaneous activity of Subject 1	49
3-2 Raster plots for Subject 2.....	50
3-3 Raster plot for Subject 3	51
3-4 Spike frequency over time for Subjects 1 and 2.....	52
3-5 Spike frequency over time for Subject 3.	53
3-6 Resistance traces from Subject 1 during 10 μ A/10 Hz current.....	54
3-7 Resistance traces from Subject 2 during 10 μ A/10 Hz current.....	55
3-8 Resistance traces from Subject 3 during 5 μ A/10 Hz current.....	56
3-9 Resistance traces from Subject 3 during 10 μ A/10 Hz current.....	57
3-10 Comparative analysis for Subject 1 during application of 10 μ A/10 Hz current.....	58
3-11 Comparative analysis for Subject 2 during application of 10 μ A/10 Hz current.....	59
3-12 Fourier power spectrum of the moving average trace for Subject 1 during application of a 10 μ A/10 Hz current	60
3-13 Fourier power spectrum of the moving average trace for Subject 2 during application of a 10 μ A/10 Hz current	61

3-14	Fourier power spectrum of the moving average trace for Subject 3 during application of a 5 $\mu\text{A}/5$ Hz current.....	62
3-15	Fourier power spectrum of the moving average trace for Subject 3 during application of a 10 $\mu\text{A}/10$ Hz current.....	63
4-1	Moving average trace for Channel 36 of Subject 2 during application of 10 $\mu\text{A}/10$ Hz current.....	74
4-2	Raster plot for Subject 2 during application of 10 $\mu\text{A}/10$ Hz current highlighting Channel 36	75
4-3	Image of four channels from the oscilloscope during Subject 1 recordings with current.....	76
4-4	Alternate resistance traces for Subject 1 during application of current.....	77
4-5	Alternate resistance traces for Subject 2 during application of current.....	78

Abstract of Dissertation Presented to the Graduate School
of the University of Florida in Partial Fulfillment of the
Requirements for the Degree of Master of Science

IDENTIFICATION OF NEURAL ACTIVITY IN *APLYSIA* ABDOMINAL GANGLIA USING
IMPEDANCE MEASUREMENT

By

Hany Elmariah

May 2007

Chair: Thomas DeMarse
Major: Biomedical Engineering

The development of a technique to effectively measure neural activity *in vivo* with high spatial and temporal resolution is among the major challenges currently facing neurophysiologists. A promising solution to this problem is the use of impedance tomography to indirectly measure neural activity through inherent changes in resistivity of active neural tissue. In order to demonstrate the viability of this solution, a consistent correlation between neural activity and neuronal impedance must be verified. I investigated this relationship using neural activity recorded from *Aplysia* abdominal ganglion with a 60-channel microelectrode arrays (MEAs). In each trial, changes in the amplitude of a sinusoidal carrier wave, the result of injecting sub-threshold AC currents at amplitudes ranging from 10-40 μA , were analyzed to determine the spatiotemporal characteristics of impedance changes in the tissue. Changes in impedance were compared with the neural activity independently measured using a MEA. The impedance results and the action potentials from the MEA were then analyzed in search of spatiotemporal correlations between each measure. Spontaneous neural activity with patterns similar to those reported in the literature were successfully recorded from the varied cell bodies within the abdominal ganglion. I then compared impedance with activity from the MEA in both

the frequency and time domain finding only a modest change in impedance during the production of action potentials in the ganglion. Future directions are suggested which may improve the resolution of this method.

CHAPTER 1 INTRODUCTION

From the primitive bottom dwellers of the ocean to the most advanced organisms on earth, virtually every member of the animal kingdom is linked by a common bond: the nervous system. In all such organisms, the nervous system is crucial in controlling basic processes such as breathing and hunger, as well as more advanced processes such as coordination and cognitive thought. One of the key issues, however, is the understanding of how the structural foundations of the nervous system produce their characteristic function (i.e., structure-function relationship). This problem can be approached from a number of varied strategies arising from a reductionist approach that begins at the basic building blocks of the nervous system, the neuron, studying the chemical communication between neurons, such as neurotransmitters and growth signaling [1-3]. Meanwhile, others have focused on the anatomical structures of neural tissue [4-6], or on the electrophysiology of individual neurons. However, in order to understand how the structure of these individual building blocks leads to their functional outcomes (behavior) it is clear that more information is needed about the activity across much of the network rather than the individual neurons themselves. Technology that can provide information from both the network and individual neurons with high spatial and temporal resolution would be invaluable.

The basic building block of the nervous system is the neuron. A neuron consists primarily of dendrites, the soma (cell body), axons, synapses, and ion channels. The soma is the main body of the neuron. From the soma extend a number of branching protrusions called dendrites which serve to receive electrical signals and transmit them to the soma. Similarly, axons also extend from the soma. These axons function to transmit electrical currents from the soma to another neuron. The inter-neuronal junction which connects an axon of one neuron to the dendrites of

another neuron is known as the synapse. Ion channels, through which ions are selectively allowed to flow, are dispersed throughout the cell membrane of the neuron [7]. This collection of fundamental units forms a dense network of interconnectivity that provides the foundation for the structure-function relationship.

At rest, the environment of the soma of a single neuron is not electrically neutral. The channels of the cell selectively block and permit the flow of charged ions through the cell membrane. Most importantly, these channels allow the flow of sodium and potassium ions. An energetic mechanism known as the “sodium potassium pump” pushes potassium into the cell and sodium out of the cell in order to maintain a negative resting potential. When a neuron is stimulated, such as by an electrical current, the sodium channels are opened, which allows sodium ions to flow down their electrochemical gradient into the cell. This depolarizes the cell, increasing the potential to values greater than 0 volts. This voltage increase triggers the potassium channels to open which allows potassium to flow out of the cell. Meanwhile, the sodium channels begin closing. As such, ions are now only flowing out of the cell, returning the soma to resting potential. This process of depolarization and repolarization as the result of stimuli is called an “action potential.” From the soma, action potentials travel down the axon to the synapse. This triggers the release of chemical neurotransmitters and ions which stimulate the dendrites of another neuron, and the process begins again [7].

Methods for Studying Electrophysiology of Multiple Neurons

The work of Bernstein, Curtis, Cole, Hodgkin and Huxley resulted in an understanding of neuronal electrophysiology and the means by which neurons directly communicate with one another. This has set the foundation for today’s researchers to focus on how multiple neurons work together as a network in complex neural systems. Current research requires measuring techniques which can record field potentials and activity patterns from large numbers of neurons.

The ideal measuring technique would encompass a wide spatial area with high temporal and detailed spatial resolution, starting from a single neuron up to the entire brain. Unfortunately, no single technique exists which fulfills this ideal.

Three of the most popular imaging techniques are electroencephalography (EEG), functional magnetic resonance imaging (fMRI), and microelectrode array (MEA) recordings. Each of these methods is useful for certain tasks, yet none of them represent a complete solution to the difficulties of studying electrophysiology, especially across a network. Each represents tradeoffs between the area that can be imaged, the spatial resolution within that area, and the temporal resolution they provide. Despite their utility, every technique used to study electrophysiology is hindered by inherent limitations of the techniques used to indirectly detect neural activity.

One of the most commonly used methods to measure activity from large areas of neural tissue is EEG. First developed by Hans Berger [8], this technique is noninvasive, using electrodes positioned on the outer surface of the scalp. The electrodes measure the extra-cellular potentials of the neural tissue, electrical fields [8], creating a spatiotemporal map of the activity of the brain. Using EEG, researchers can monitor global fluctuations in extra-cellular potentials, particularly EPSPs (excitatory post-synaptic potentials) and IPSPs (inhibitory post-synaptic potentials), of different regions of the brain during various activities or events. EEG has been used to evaluate the electrophysiological causes of neural disorders, such as epileptic seizures, including where the seizure begins and the pattern by which it propagates [9, 10]. Another application of EEG is to correlate neural activity with certain behaviors, such as voluntary movement, in order to develop brain-machine interfaces [11-13]. EEG can also be used to elucidate neural activity during sensory input [14, 15] and sleep studies [16, 17].

EEG measurements are characterized by good temporal resolution, but are also hindered by weak spatial resolution. With relatively large electrodes placed on the scalp, the resolution is limited by the physical proximity of the electrodes to one another. This limitation is furthered by the fact that EEG electrodes detect field potentials from a wide surface area (about 10 cm²). Placing two electrodes within this area will result in the simultaneous detection of field potentials by both electrodes. The spatial resolution of this technique is further limited by the multiple layers of tissue between the electrodes and the brain (blood vessels, dura, skull, skin, etc.). These layers attenuate the signals, attenuating and distorting the observed surface potentials and completely eliminating potentials from deeper brain layers. As a result, the activity recorded using EEG is reduced to a spatial average of activity, rather than a detailed, spatially localized observation of specific neurons [8].

To improve spatial resolution, other methods have been developed which also can indirectly image neural activity, such as fMRI, a method closely related to traditional magnetic resonance imaging (MRI). The MRI was developed as a noninvasive means to image the structural information of tissue. The technique is based on changes in the dipolar relationship of water molecules in almost all living tissue and their interaction with magnetic fields. The magnetic field applied during the MRI causes these dipoles to align, and they are then perturbed by application of radiofrequency energy. As the dipoles recoil to their resting position, they emit energy which is then imaged. One of the advantages of this technique is that it can provide relatively high spatial resolution (< 1 mm). While MRI is useful in mapping neural anatomy, it is inadequate to measure any structural-functional relationships because this technique does not provide any information about the neural activity within the areas that are imaged [8].

Ogawa, et al. [18] noted that cortical blood vessels are more clearly visible as blood oxygen decreases due to the resulting changes in the magnetic field. Moreover, neurons require a great deal of energy during activity, a process which utilizes significant amounts of oxygen. This creates notable discrepancies in the oxygen concentrations in the arteries near the active neurons as compared to the nearby veins. Putting these facts together, Ogawa concluded that directly imaging changes in oxygen concentration can indirectly produce an image of neural activity. This new method for using MRI to study neural function is appropriately titled fMRI [8, 19, 20]. Like EEG, fMRI is useful for creating spatiotemporal maps during various neurological states. For example, fMRI has been used to study neural physiology of various emotional states [21, 22], body movement [23], and verbal comprehension [24].

Neural imaging with fMRI provides some notable advantages. Most importantly, like MRI, it provides high spatial resolution. Like EEG, the technique is also non-invasive. There are some significant limitations. The specific physiology behind the altered levels of blood oxygen in the vessels, and the ensuing ability to indirectly image activity, is not known. While fMRI can determine the existence of activity at a spatiotemporal location, it cannot determine the type of activity (excitatory, inhibitory, action potential propagation, etc.). The indirect nature of fMRI imaging creates the potential that unique processes and states of neuronal activity may nonetheless result in one common state of the blood oxygen levels in the vessels. In such situations, the fMRI is unable to distinguish between the various neuronal activity states, a problem that is also shared with the field potentials using EEG. Finally, there is a delay between the occurrence of neural activity and the ensuing use of oxygen by the neuronal tissue. Thus, multiple frames of images must be integrated over time to detect any changes which decreases the temporal resolution of this technique [8].

Another method which provides much higher spatial and temporal resolution is the MEA. An MEA consists of a grid of multiple electrodes, each of which has a diameter on the order of 50 microns or more. These electrodes are able to record extracellular potentials from multiple spatial locations simultaneously. A wide variety of electrode arrays have been developed following this basic idea including arrays such as microwire bundles, shaft electrode arrays, flexible grid electrodes for *in vivo* applications and planar arrays for *in vitro* studies. Figure 1-1 shows an example of an array from Multichannel Systems designed for *in vitro* work. The MEA is square in shape and fitted with a small, cylindrical dish centered on its face which contains the tissue and medium used to support it. The electrode grid is embedded in the center of this dish. The electrodes are made of either titanium nitride or platinum, depending on the application. A series of 60 contact pads, made of either titanium or indium tin oxide, are embedded along the perimeter of the MEA. These are connected to the electrodes via conductive tracks such that the electrical signals may be sent from the tissue to the electrode and then to the contact pads through the tracks. From the contact pads, signals are amplified with a filter amplifier and then, finally, sent to the data acquisition computer [25]. This style of MEAs has been used for studying pharmacology [26, 27] neural regeneration [28], synaptic plasticity [29, 30], visual perception [31, 32], and robot control [33, 34]. Additionally, MEAs have been used extensively for studies in the field of cardiology [35, 36].

Because MEAs directly record extracellular potentials at a reasonably high sampling frequency, this technique boasts very little time delay and good temporal resolution. Spatially, MEAs can record field potentials or even record from individual neurons. Spatial resolution is limited by the number of electrodes that can fit on the surface of the MEA. The smallest electrode size available on MEAs is currently 10 μm , so the spatial resolution cannot be more

precise than 1 electrode in a 10 μm area. Resolution is further limited by the fact that each electrode records spike activity from an area of tissue, not an infinitesimally small point. Each electrode detects spikes from a radius of 100 μm . Even placing the electrodes as close as physically possible will simply result in repetitive detection of potentials. The most obvious disadvantage of MEAs is their inability to record from large-scale tissue samples, such as an entire human brain. At most, a planar MEA such as that shown in Figure 1-1 can be applied to recordings from small slices of neural tissue. For larger tissue samples, clinical methods such as EEG, fMRI, etc. are required [25].

Impedance Tomography

Impedance tomography is a relatively new modality which is used to image the electrical impedance of a tissue sample. Electrodes are placed in a ring around the tissue sample. One pair of electrodes is used to propagate a test current, while the rest of the electrodes are used to record the resulting voltages. This technique is repeated in varying orientations through the tissue. A reconstruction algorithm is then used to create an image of the impedance throughout the tissue sample. Technically, only four electrodes are necessary to obtain enough information to create an impedance map. However, spatial resolution is dependent upon the number of electrodes. The final images created are generally two-dimensional slices [37]. This technique has a number of applications including monitoring lung function [38, 39] and detecting various types of cancer [40, 41].

Ion Channels and Neuronal Impedance

Early evidence of the role of ion channels for propagating electrical signals in neurons came from studies in the first half of the twentieth century of impedance within the neural tissue. In 1902, with knowledge of the electrical potential gradients across the neuronal membrane, Bernstein hypothesized that neural activity occurred when this gradient disappeared as a result of

increased permeability of the membrane to ions. This hypothesis came as the result of mathematical analysis using the Nernst equation, by which Bernstein came to the belief that, during activity, the membrane became completely permeable to all ions and resulted in a depolarization of the cell to 0 volts [42].

Experimental support for Bernstein's hypothesis was later established by Curtis and Cole in 1939 [43]. In those experiments, Curtis and Cole studied impedance within the squid giant axon. The pair extended the axon and stimulated from one end, allowing propagation of a current to the other end. Meanwhile, they measured the transverse impedance with electrodes positioned on each side of the axon and an oscillograph. The results showed that the impedance within the axon did, indeed, change during activity. In fact, Curtis and Cole found a 30-40 fold increase in the conductance of the axon during action potentials. They also found that there was a slight delay in the impedance change. Rather than an immediate change in conductivity occurring in unison with the depolarization phase of the action potential, the impedance decrease was found to occur in conjunction with the repolarization phase and the decrease in the depolarizing electromotive force.

Since the studies of Curtis and Cole, other researchers have further elucidated the relationship between impedance and activity in neural tissue. Most importantly, in 1952, Hodgkin and Huxley were finally able to determine the permeability of channels to various ions throughout the course of action potentials [44-48]. The key to their success was their application of a new space clamp technique. For this method, a conductive wire was threaded into the axon. This brought the entire length of the axon to the same electrical potential. Thus, the position of the measurement on the axon became irrelevant, and Hodgkin and Huxley were able to study the temporal changes of current flow and conductivity across the membrane [43]. Through these

studies, Hodgkin and Huxley created a set of differential equations which modeled the behavior of neurons during action potentials, the basis of our current understanding of ion channel behavior and permeability during activity.

Since the Nobel Prize-winning breakthroughs of Hodgkin and Huxley, researchers have continued to focus on current flow and impedance in neurons. It has been shown that, at low frequencies, neuronal membranes are essentially non-conducting. Any applied, external current will flow exclusively through the extra-cellular space, and intracellular conductivity will ostensibly be zero [49-53]. During activity, as the voltage gated channels in the membrane are opened, causing depolarization and then repolarization, the impedance of the neuron decreases and allows current to move intracellularly. Such changes have been observed in cats [54, 55], rabbits [56, 57], rats [58, 59], and even human neural tissue [60, 61].

The direct correlation between impedance shifts and neural activity has been challenged, at least in part [62]. In studies using implanted cortical electrodes in cats, Klivington and Galambos demonstrated that shifts in impedance within neurons occur only in conjunction with action potentials. Moreover, these same studies demonstrated that the shape of the impedance shift is constant when it does occur and, thus, independent of the shape and magnitude of the associated action potential. They also found that action potentials may occur in the absence of any detected shift in neuronal impedance. It is not clear whether impedance may be a viable alternative to other imaging techniques for neural activity.

Experimental Goals

The purpose of my study was to determine whether resistance changes can be correlated with neural activity. In other words, can resistance information be used as a unique method to measure and identify neural activity across a small population of neurons? To accomplish this, neural activity was independently recorded using MEA technology and compared with the

activity measured using impedance tomography. For preliminary studies, I studied the abdominal ganglion of *Aplysia californica*, a small sea slug. Figure 1-2 shows a diagram outlining the major cell bodies found in the abdominal ganglion. The ganglion consists of two hemispheres (labeled as “L” and “R”) of cells which are held together by connective tissue and covered by an insulating sheath. These hemispheres are further subdivided into the left rostral quarter-ganglion (LRQG), right rostral quarter-ganglion (RRQG), left caudal quarter-ganglion (LCQG), and right caudal quarter-ganglion (RCQG), in which the ganglion neurons are located [63]. One of the primary advantages of using this ganglion is that distinct patterns of activity are produced by each area of cell bodies. Hence, the activity recorded from both the MEA and impedance tomography can be localized anatomically based on the activity pattern that is detected.

Studying the electrophysiology of *Aplysia* abdominal ganglion using MEAs was first accomplished by Novak and Wheeler in 1986 [64]. In those studies, action potentials were recorded from the ganglion cells using a 32 electrode, planar MEA. The ganglion is surrounded by an insulating sheath; for this reason, Novak and Wheeler measured only from the dorsal surface of the ganglion, over which the sheath is thinner compared to the ventral side. They reported three patterns of activity, which they used as a criterion to divide the right dorsal ganglion into three groups: cells around R15, the RB/RC region, and the white rostral cells (Figure 1-2). R15 can be observed in the RCQG (blue region). Lateral and rostral (above and to the right on the figure) to R15 are two clusters of cells, identified as RB and RC. The white rostral cells can be observed even further rostral, in the RRQG (yellow region) [63]. Results showed that neurons near the R15 neuron fire with rhythmical bursts of activity once every 10 seconds (0.1 Hz). In the regions near RB and RC, rapid firing, near 2 Hz, was observed. Finally,

Novak and Wheeler observed firing rates of 0.5 to 1 Hz in the rostral white cells. These results are summarized in Table 1-1 [64].

In light of those studies, we have used a 60 channel MEA in order to observe ganglion activity with unprecedented resolution. Further, we have applied this technique for the novel purpose of observing resistance shifts during action potentials. Specifically, we injected the ganglion cells with a constant AC current during each trial while recording voltages with the MEA. Using a constant current source, the resistance can be calculated by simply dividing the measured voltages by the amplitude of the current, as defined by Ohm's Law. This value was calculated over the duration of each trial using a method combining synchronous demodulation and a moving average algorithm. Meanwhile, a spike detection algorithm was used to determine the spatiotemporal location of action potentials in the neural tissue. Spatiotemporal patterns of resistance changes were then compared to spatiotemporal patterns of neural activity in hopes of showing that action potentials are generally accompanied by changes in neuronal resistance, and vice versa.

In the following experiment, the neural activity from the abdominal ganglion was assessed in three animals using planar MEA technology. A sinusoidal current source was then injected into the MEA using external electrodes to image activity using changes in resistance that could be correlated with the activity detected via the MEA. This experiment tested four different current amplitudes ranging from 5 to 40 μA to determine which current level provides the best resolution. Consistent and reliable changes in resistance that correspond with changes in activity would provide support for the viability of this technique for future studies.

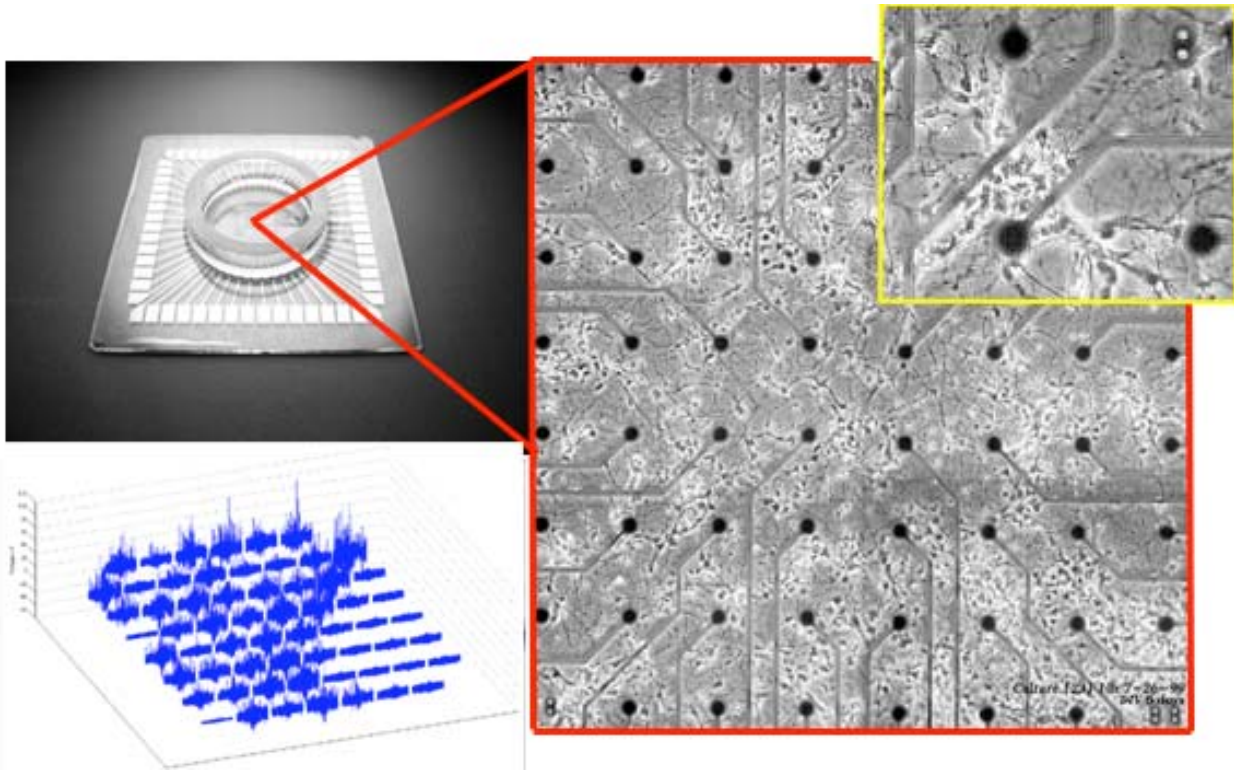


Figure 1-1. Image of a standard microelectrode array from Multichannel Systems. This 60 channel array consists of $30\ \mu\text{m}$ electrodes spaced $200\ \mu\text{m}$ apart. Each electrode can measure the electrical changes produced during action potentials of neuronal tissue. The right panel shows an example of an MEA with dissociated rat cortical neurons. The lower left panel shows an example of an 8×8 grid of extracellular potentials recorded from neurons (200 ms window for each electrode).

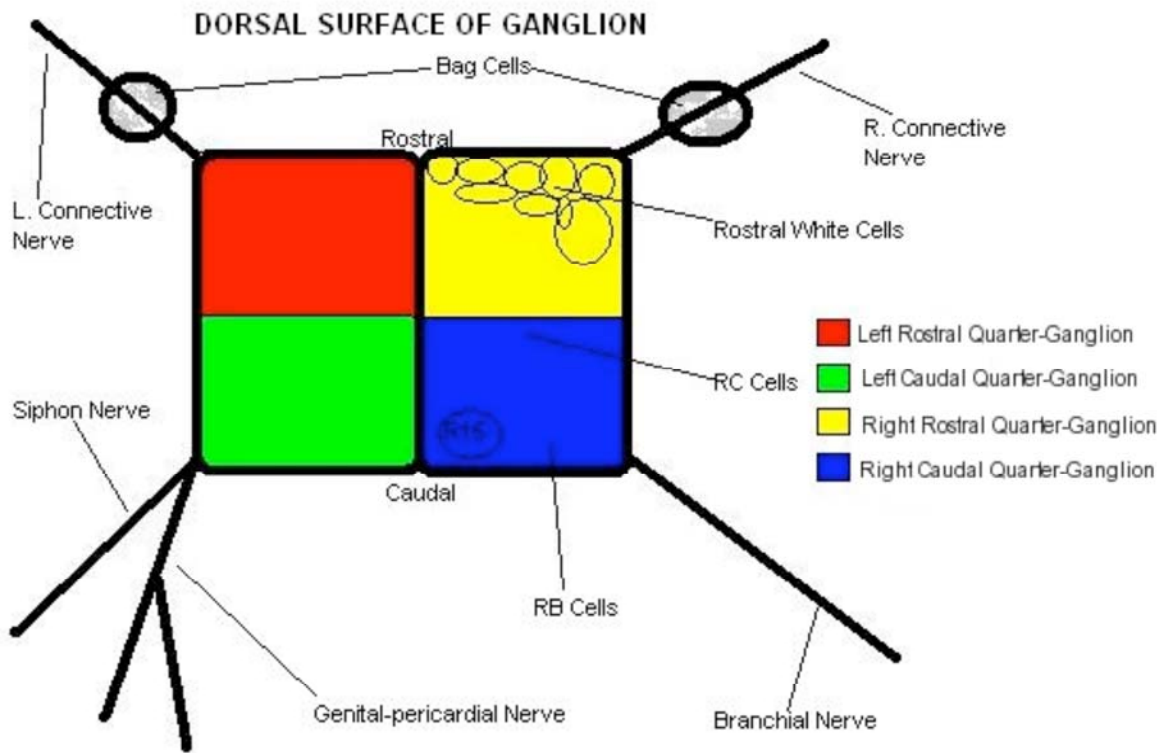


Figure 1-2. Diagram of the dorsal surface of the abdominal ganglion. The neuropils, which lie dorsal to each hemisphere, have not been included in order to show the neurons.

Table 1-1. Summary of firing patterns observed for three primary cell groups on the dorsal surface of the abdominal ganglion [64].

Cell Group	Pattern of Firing	Frequency (Hz)
R15/surrounding cells	Bursting	0.1
RB/RC	Irregular	2
White Rostral Cells	Regular	0.5-1.0

CHAPTER 2 MATERIALS AND METHODS

***Aplysia* Preparation**

Aplysia californica for all experiments were obtained from the NIH *Aplysia* facility at the University of Miami. For each set of experiments, the animals were delivered the week preceding experimentation and then stored in a 10-gallon saltwater tank. The tank was filled with regular tap water and then a commercial aquarium salt mix was added. The salinity was measured with a hydrometer and adjusted to a level of 33.5 ppt with a specific gravity of 1.024 at room temperature (75 degrees Fahrenheit). To neutralize chemicals in the water which could potentially harm the *Aplysia*, 5 mL of a commercial water conditioner was added to the tank. A water pump was then attached to the side of the aquarium to circulate the water. While kept in the tank, the animals were fed a piece of iceberg lettuce every 1-2 days.

Preceding each set of experiments, the abdominal ganglion of an *Aplysia* was surgically removed. First, a solution of 77.05 g/L of MgCl₂ and 3.5745 g/L of HEPES buffer was made for use as an anesthetic. The animals were placed on a foam plate with the animal's lateral side facing up. The anesthetic was injected into the foot process, middle, and head. As a defense mechanism, *Aplysia* may release ink during the injections. In order to avoid this, the animal was first injected with 5 cc of anesthetic with a 1 cc syringe through a 28G1/2 needle. Five injections were made into the foot process, followed by the middle, and finally the head. This technique was repeated such that a total of 20-25 cc of anesthetic was injected into the organism through the small gauge needle. After these first injections, it is safe to use a large, 16G1/2 gauge needle and inject 10 mL of anesthetic with each injection. Again, the anesthetic was injected at the foot, middle, and head. This technique was repeated until the animal was non-responsive to physical

stimuli and body movement had ceased, generally a total of approximately 80 mL of anesthetic. All injections were made perpendicular to the longitudinal axis (with the needle pointed down into the foam plate). This prevented the anesthetic from being injected into the abdomen and damaging the ganglion.

Once the specimen was anesthetized, the surgery proceeded with a mid-dorsal, longitudinal incision from the foot process to the head. A scalpel was used to gradually dissect the connective internal connective tissue. As necessary, the skin was pinned back in order to expose the abdomen of the organism, allowing access to the ganglion. The ganglion can be identified as a small, orange bundle in the center of the abdomen. It is held in place by nervous tissue, which was detached with a razor blade or a scalpel. Care was taken to preserve the axons protruding from the ganglion. With the naked eye, there appear to be four such axons, approximately evenly spaced around the circumference of the circular surface of the ganglion. However, one of these axons is thicker than the other three and is, in fact, two closely positioned axons. This “double” axon can be used as a marker for positioning the ganglion [63].

The unused *Aplysia* tissue was placed in a designated biohazard bag and sealed for disposal. The bag was placed in a biohazard waste box for proper removal by the University of Florida Office of Environmental Health and Safety. All gloves, syringes, razors, etc. used in the procedure were also disposed as biohazard waste in compliance with the NIH/CDC guidelines, the State of Florida Administrative Code 64E-6, and restrictions of the Alachua County landfill.

Microelectrode Array Setup

Recording from the *Aplysia* abdominal ganglion employed a "3-D" microelectrode array from Ayanda Biosystems in Lausanne, Switzerland. These MEAs are ideal for recording from thick pieces of neural tissue, such as cortical slices, hippocampal slices, and ganglion cells for a multitude of applications such as neuroplasticity, visual perception, and impedance studies. The

electrodes in the dish are shaped with a three-dimensional orientation to better penetrate the deep layers of tissue. In Figure 2-1, the electrodes are magnified to show their raised, conic shape which penetrates into deep tissue. The electrodes are aligned in an 8x8 grid (with the corners removed) and are separated by 200 μm . Each electrode is 50 μm high with a diameter of 40 μm at the base which comes to a fine point at the tip. The electrodes, tracks, and contact pads are all composed of platinum, and the MEA is insulated with SU-8.

As the spatial activity patterns of *Aplysia* abdominal ganglia are well documented, it is useful to deliberately orient the neurons on the surface of the MEA. While looking down at the MEA, the “Ayanda Biosystems” logo was oriented such that it was at the top of the face of the MEA and readable from left to right (the same orientation was used when resting the MEA on the amplifier base, as discussed below). Next, the ganglion was positioned in the center of the array. Because the ganglion cells are surrounded by a nonsymmetrical, insulating sheath, the ganglion was placed such that the thinner side of the sheath was facing the MEA surface, as the thicker side may decrease the quality of data acquisition. The thinner side can be identified because it has a bright orange color, as opposed to the thicker side which has a brown appearance. The ganglion was rotated such that the “double” axon is pointing towards the bottom-right side of the MEA surface (with the “Ayanda Biosystems” logo designated as the top). In this orientation, the R15 neuron is positioned on the lower, left side of the MEA. Once the ganglion was positioned on the MEA, it was viewed under a microscope and images were taken using a Macintosh iSight digital camera (Figure 2-2). As seen in the figure, variations in the orange color (lower right) are the different cell bodies contained within the abdominal ganglion. One of the axons can be observed looping around the left hand side of the image outside the electrode grid.

In order to improve the adhesion of the ganglion cells to the MEA, the MEA was treated with polyethyleneimine (PEI). The treatment was performed under a sterilized fume hood. Using a micropipette, 100 μ L of PEI was deposited on the surface of the MEA. This small quantity of PEI was left on the MEA for approximately 30 minutes and then removed from the surface using a fine tipped vacuum. Care must be taken in this step not to damage the leads of the electrodes on the bottom of the MEA. After treatment with PEI, the dish was further rinsed with ultra-purified water, from a Millipore Simplicity 185 purifier, using the same procedure. However, the procedure is repeated 10 times, such that 1 mL of water is used in the process.

For the maintenance of activity in the extracted neurons, the ganglion was placed in an artificial seawater (ASW) bath in the MEA. The bath closely resembles the seawater conditions in which the *Aplysia* usually live, allowing the neurons to remain physiologically active for up to 8 hours. The bath consisted of 26.8824 g/L NaCl, 0.7753 g/L KCl, 11.1815 g/L MgCl₂, 1.221 g/L CaCl₂, and 3.5745 g/L of HEPES to maintain a pH of 7.8.

During experiments, a fitted Teflon lid is placed around the MEA dish. The lid is equipped with 4 electrodes, which are equally spaced around the circumference of the ring. Two opposing electrodes were used to propagate the measuring sine wave from an electrical stimulus generator. In order for these electrodes to successfully send and receive current, the ASW solution was filled to the top of the lid, creating a conductive path for electricity. In order to prevent leakage of the ASW between the dish and the lid, a fitted rubber O-ring was placed in the intervening crevice.

Data Acquisition

An MEA1060-BC amplifier from Multi Channel Systems was used to record neural activity. This amplifier was designed specifically for MEAs possessing a special base on which to rest the MEA and a series of pins which make direct connect with the contact pads of the

MEA. The amplifier is connected to a data acquisition A/D card which collects the data and then outputs it to a computer for processing. The sampling rate used was 25 kHz with a bandpass of 0.1-10 kHz. At this sampling rate, the length of recordings is limited largely by storage capacity as a single 200 second data file requires approximately 800 MB of hard drive space.

Experimental data was collected from the data acquisition card on a PowerMac dual G5 desktop. A software bundle called “MEA Bench,” developed by Dr. Thomas DeMarse for Mac OS X, was used to perform a number of powerful functions for data acquisition and analysis. Most notably, for these experiments, the “scope” and “spike detector” functions proved to be the most useful. The scope program serves as an on-screen oscilloscope. The data can be observed in real time as it is collected, saved, and then replayed. All of the MEA channels are displayed simultaneously, with a function to zoom in on any specific channel(s) or adjust the voltage and time scales as appropriate. As seen in Figure 2-3, aside from the four corners, each window on the oscilloscope represents one of the digital MEA channels. The four corners display analog channels; most notably the top left corner outputs a square wave in phase with the injected sinusoidal current. The icons at the top of the window allow the user to control time scale, voltage scale, and to freeze and rewind the data. Figure 2-4 shows a magnified image of one of the channels during an action potential (highlighted in red). The window shows 200 ms of data with a voltage scale of 50 μ V on the vertical axis. The spike detector will be described in more detail below.

A sinusoidal measuring current was used to measure changes in the impedance of neurons in the ganglion. This current was produced by an STG 1008 stimulator from Multi Channel Systems. This stimulus generator is capable of producing sinusoidal, square, monophasic, biphasic, and ramp waveforms with a voltage range of -8 to 8 V and a current range

of -0.8 to 0.8 mA. The output signal is controlled using MC_Stimulus, and included a software package with which the user can set the stimulus parameters and then upload them to the hardware. The stimulator was connected to the electrodes which were implanted in the Teflon ring using standard alligator clips. Hence, the measuring waveform was propagated through the ASW and the tissue. Figure 2-5 shows a schematic of this setup. The MEA is at the bottom of the image, with the Teflon lid fitted around the dish. The electrodes are embedded within the ring (left and right sides of the figure) such that the current can propagate from one side to the other. The lid is filled with the ASW solution as shown, with the tissue resting at the bottom on the MEA dish.

A flow diagram of the setup of the recording apparatus in Figure 2-6 shows the stimulator connected to the electrodes on the MEA lid to send a current into the dish, while the MEA electrodes record voltages and send the information to the amplifier. When positioned on the MEA in the ASW solution, the ganglion cells spontaneously fire. For this reason, none of the recordings discussed here employed a stimulating current to elicit action potentials. Instead, all injected currents used were sub-threshold. Each current can be described by its amplitude and frequency, parameters which were controlled to obtain the most useful data.

A key factor of the measuring current is that it must propagate at a low frequency. At high frequencies, the current is able to penetrate the intracellular space through the cell membrane of an inactive neuron. Conversely, low frequency currents are trapped in the extracellular space, unable to cross the membrane [52]. Yet, during cellular activity, the conductivity increases by 30-40 times [43], allowing either current to move into the cell. Hence, the low frequency current demonstrates a higher measurable impedance change in the neuronal cell membranes. However, at low frequencies, the current amplitude necessary to stimulate action

potentials is lower than for high frequency currents. Thus, 10 Hz currents were used in these experiments to maximize the measurable impedance change, at amplitudes of 5, 10, 20, and 40 μA to avoid stimulation.

In addition to injected current recordings, baseline recordings of spontaneous activity were obtained for each specimen. These recordings are useful in observing the natural, spontaneous activity of the neurons. Specifically, these recordings were used as a reference point with which to determine if the injected current recordings were, indeed, sub-threshold.

Three specimen were used for separate experimental trials. Four separate trials were performed for each specimen. First, 200 seconds of baseline activity was recorded. Then, 200 seconds of data was recorded for each of three current values. For Specimens 1 and 2, currents of 10, 20, and 40 μA were used, all at a frequency of 10 Hz. The same procedure was used for Specimen 3, though an added trial was included using a current of 5 μA at 10 Hz.

Data Analysis

Least-Mean-Square Adaptive Filter

Before an analysis of impedance could be conducted it was necessary to first identify any neural activity embedded in the 10 Hz sinusoidal wave so that the timing of these events could be compared with any changes in impedance. Applying the typical spike detection method would be useless given the large amplitude fluctuations produced by the 10 Hz sinusoidal current. Hence, the waveform from the current source must be separated from those produced by the action potentials of the abdominal ganglion. To accomplish this, a least-mean-square (LMS) adaptive filter was used to remove the 10 Hz sinusoidal currents [65] before spike detection occurred. The LMS filter is a simple tool which can compare an input waveform to a desired waveform and then output the error between the two. For example, in these experiments, the input waveform was a sinusoidal wave recorded during propagation through the neural tissue

(which included neural data and noise). The desired wave used, then, was the 10 Hz sinusoid that was initially injected into the neural tissue (without the neural activity). The LMS algorithm then outputted the error between these two waveforms which, ideally, is equivalent to the neural activity and the noise which would have been observed during a baseline recording without a sinusoidal carrier current. The top panel of Figure 2-7 shows a baseline recording with a prominent action potential at 0.975 seconds. The middle panel shows an example of a recording during application of the current. Potentials recorded from the tissue (including action potentials) are visibly embedded on the wave, though the spike detector software is unable to detect this. After filtration (bottom panel), the raw data is isolated from the sinusoidal wave, allowing for detection of action potentials with the spike detector.

The mechanism of the LMS filter is characterized by two primary functions: filtration and adaptation. During filtration, the input wave is compared to a desired waveform and then the algorithm outputs the error between the two, as previously noted. In the adaptive process, the algorithm determines the proper weights for the tap weight vector, \mathbf{w}_n . This algorithm is described by the following equations:

$$\rho = \text{filter order}, \mu = \text{stepsize}, n=1, \epsilon = \text{error} \quad (1)$$

$$\mathbf{x}(n) = [x(n) \dots x(n-\rho)] \quad (2)$$

$$\epsilon(n) = d(n) - \mathbf{w}_n^T \mathbf{x}(n) \quad (3)$$

$$\mathbf{w}_{n+1} = \mathbf{w}_n + \mu \epsilon^*(n) \mathbf{x}(n) \quad (4)$$

where \mathbf{w}_n is initialized to zero, $\rho = 10$ taps, and the step size μ was set to 0.000000001 for slow adaptation of the filter.

Spike Detection

The process of LMS filtration was necessary in order to isolate the raw neural activity. From this data, then, the spatio-temporal locations of actions potentials were determined using a spike detection algorithm. The algorithm is built into the MEA Bench software which was also used to record the data. The spike detector first calculated the standard deviation of 5 seconds of random noise at the beginning of the data set. The value obtained was then used as a threshold by which to determine the location of spikes. Any data value in the data set which exceeded five times the standard deviation from the mean was deemed a spike. Information about each spike including channel, time, height, and width was then stored to a file for further processing.

Moving Average Algorithm

In addition to action potentials, it was necessary to determine the location of impedance shifts in the neural data. This was determined from the sinusoidal carrier wave with the embedded neural data. Each injected sinusoidal current was characterized by a constant amplitude (either 5, 10, 20, or 40 μA). As this current moved through the conductive tissue, the tissue acted as a resistor. By Ohm's Law, the voltages recorded with the MEA are directly proportional to the impedance of the tissue. Hence, the impedance values were obtained by a simple division of the measured voltages by the current amplitude.

For analysis of the impedances, the sinusoidal signal was demodulated by multiplication with a square wave synchronous with the injected current waveform (recorded on one of the MEABench amplifier's analog auxilliary channels), and then estimating the resistance or reactance amplitude using a moving average algorithm. The moving average algorithm calculated the average resistance of the 10 Hz voltage data using a sliding window that was fitted to one full period of the sinusoid, approximately 2500 samples. After each calculation, the window slides by one sample and then calculates another average over one period of the wave. Hence, the final moving average vector was the same length as the original voltage data vector and displayed the average impedance of the neural tissue for each sample window.

Final analysis consisted of comparisons between the moving average data and the spike detection data. The time and location of impedance fluctuations were evaluated against spike detection data. Correlated occurrences of impedance changes and neural activity in the same location are indicative of a relationship between the two.

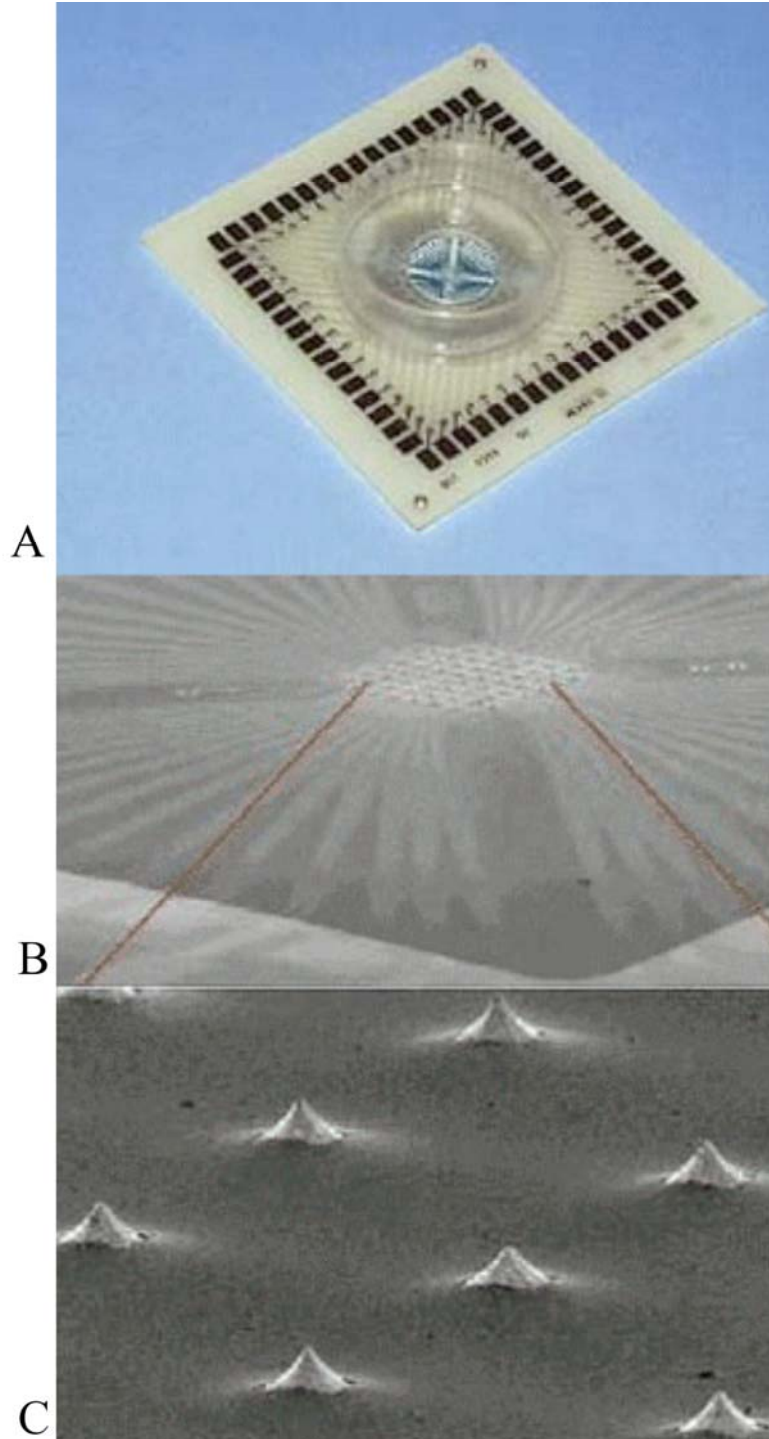


Figure 2-1. Multichannel Systems 3-D microelectrode array A) Entire Array B) Magnified image of the electrodes C) Further magnified image. This array consists of 60 electrodes separated by $200\ \mu\text{m}$. Unlike the standard planar MEA, the electrodes on these arrays consist of $50\ \mu\text{m}$ high cones which are designed to penetrate the tissue from which data is recorded and, hence, improve the signal-to-noise.

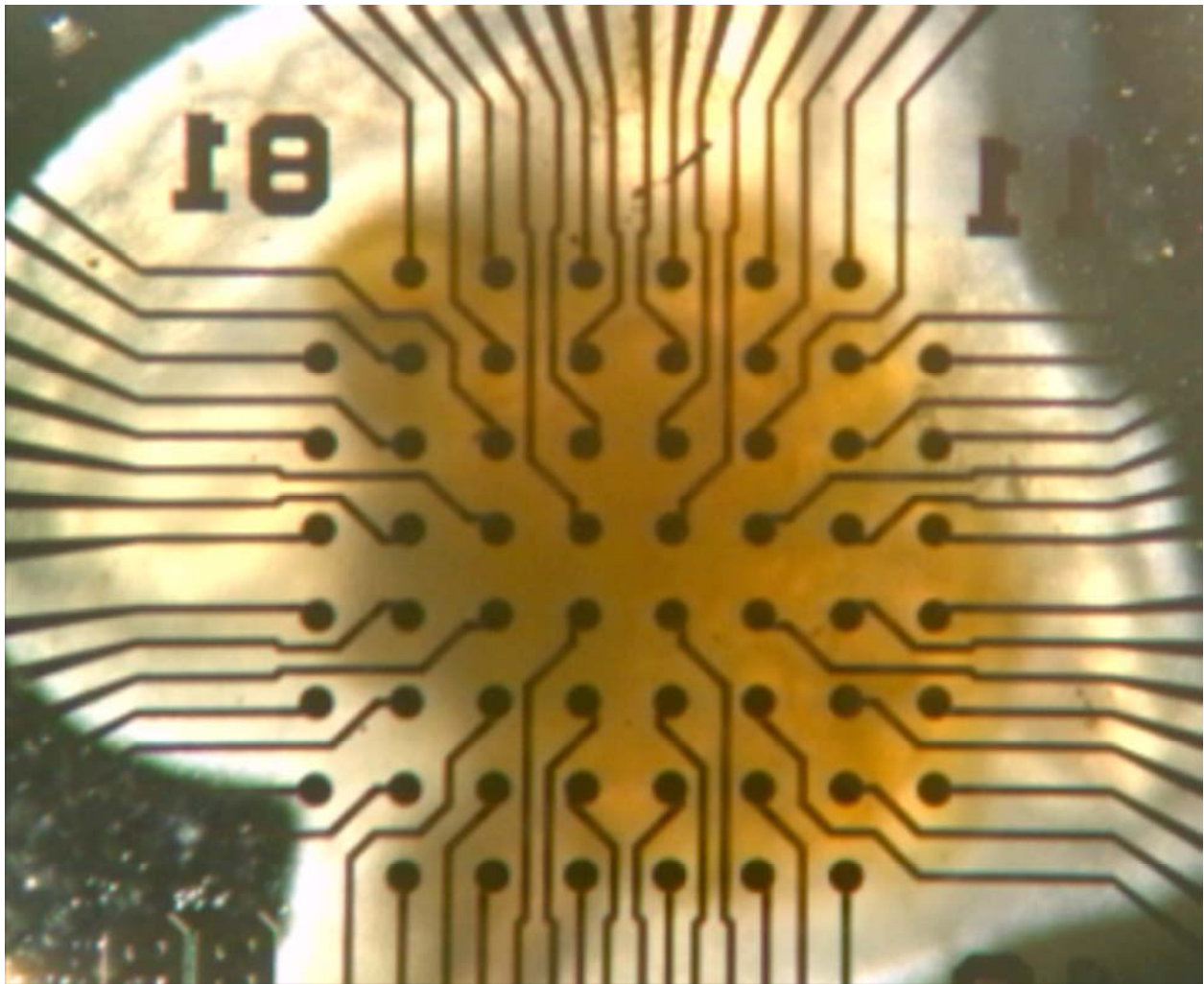


Figure 2-2. *Aplysia* ganglion centered on the dish of a microelectrode array. Although it is difficult to see, variations in the orange color (e.g., lower right) are the different cell bodies contained within the abdominal ganglion. One of the axons can be seen looping around the left hand side of the picture outside the electrode grid. (Image is from a Nikon TS-100 confocal microscope at 200x magnification.)

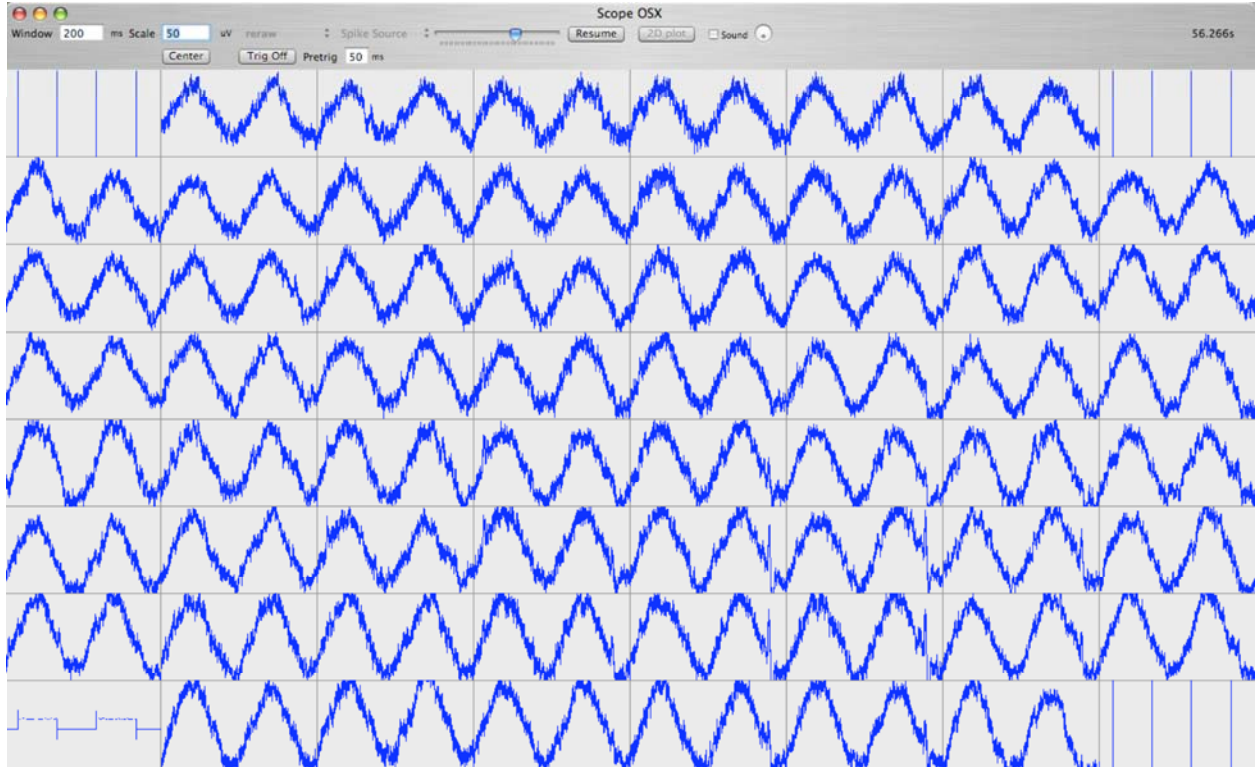


Figure 2-3. Oscilloscope function of MEABench on Mac OS X. The image shows data collected during injection of a $10 \mu\text{A}/10 \text{ Hz}$ sinusoidal current. Electrical activity from the 8×8 grid of electrodes is shown. Each window represents 200 ms of the output from one channel. The vertical scale for each window is $50 \mu\text{V}$. The data from the four corners are from auxillary channels used to record the timing of the sinusoidal current source.

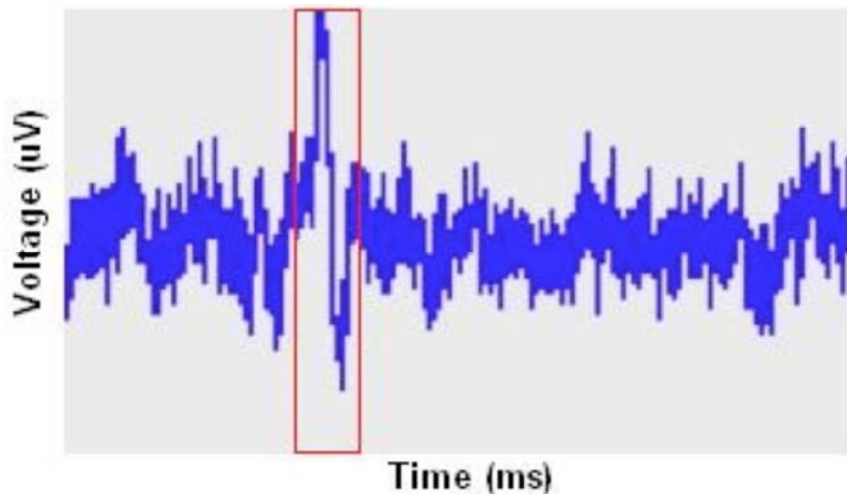


Figure 2-4. Spontaneous action potential (red box) recorded from abdominal ganglion cells and displayed on the MEABench scope tool. The window shows 200 ms of data with a voltage scale of $50 \mu\text{V}$ vertically.

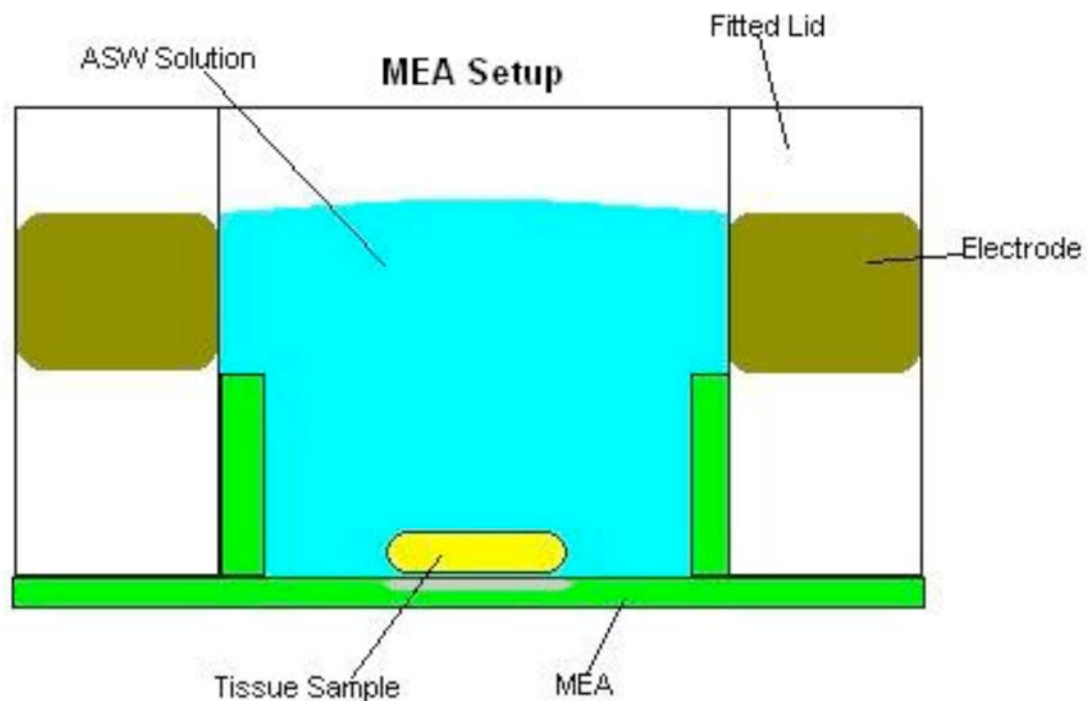


Figure 2-5. Schematic of the MEA setup. Stimulator is attached to the electrodes to propagate a current from one electrode, through the tissue/ASW, to the other electrode.

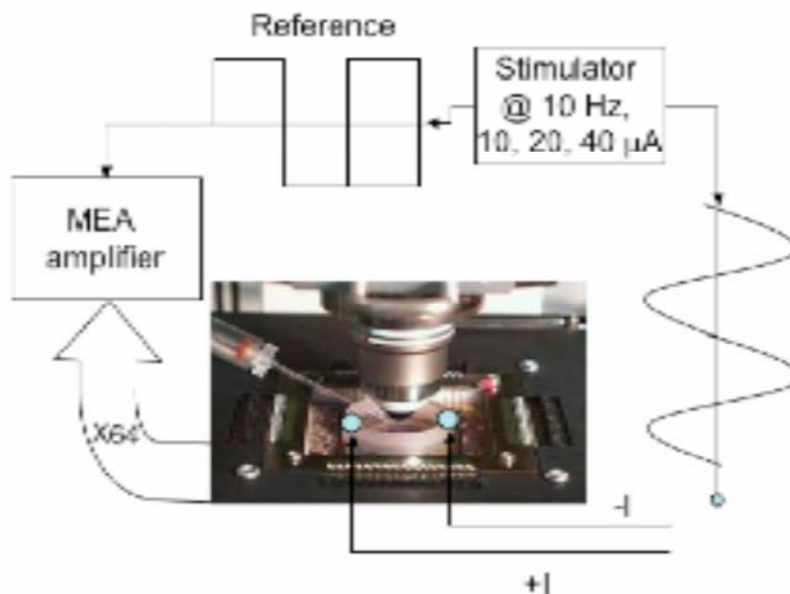


Figure 2-6. Flow diagram of the experimental apparatus. The stimulator injects currents across the tissue in the MEA. Potentials recorded by the MEA electrodes are sent to the amplifier.

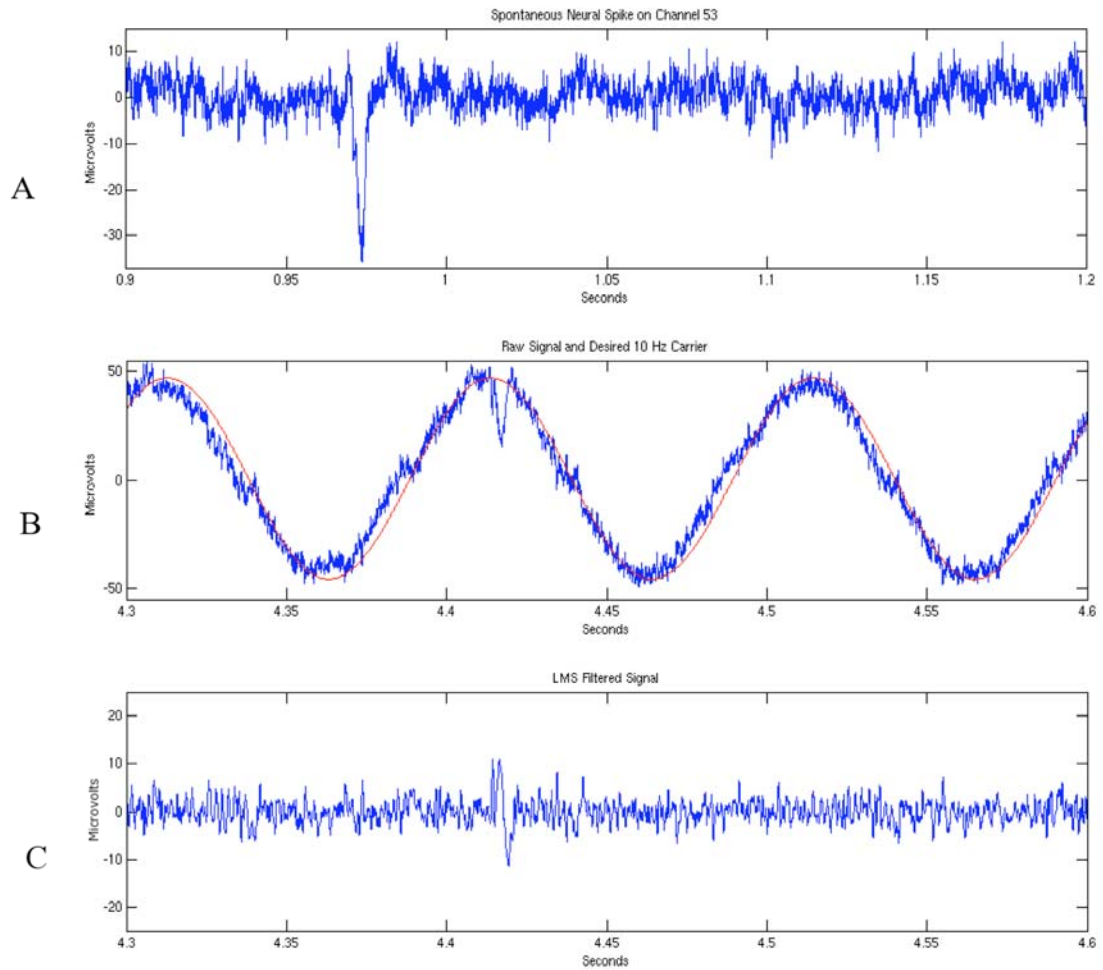


Figure 2-7. Example of LMS filtration. A) Spontaneous neural activity from *Aplysia* abdominal ganglion. B) Spontaneous neural activity during application of a $10\ \mu\text{A}/10\ \text{Hz}$ sinusoidal current. C) LMS filtration to remove the sinusoid.

CHAPTER 3 RESULTS

In this experiment, the neural activity using MEA technology from the abdominal ganglion of three subjects was compared to changes in the resistance under four different current levels, a 10 μA , a 20 μA , and a 40 μA injected current. The third subject also included a 5 μA current recording. All propagated currents were characterized by a frequency of 10 Hz. For each subject, several minutes of spontaneous activity were first recorded to characterize the activity patterns before the application of any current source. Each of the currents was then separately applied and recorded for several minutes.

Patterns of Activity

Measurements using a 60-channel MEA were successful for the purposes of displaying and detecting action potentials from the abdominal ganglion neurons. As indicated in Table 1-1, the expected results could be divided into three categories: regular activity, irregular activity, and bursting. Moreover, the frequencies of firing expected for these three categories were 0.5-1 Hz, 2 Hz, and 0.1 Hz, respectively.

In order to visually display patterns of activity, raster plots were created to show activity on all channels over time. These are scatter plots which display time across the horizontal axis and MEA channel number on the vertical axis. Each marker on the plot, then, represents the occurrence of an action potential at a specific time on a specific channel. Hence, raster plots display a spatiotemporal map of all activity measured by the MEA. Figures 3-1A, 3-2A, and 3-3A show the spontaneous activity of the abdominal ganglion before current application from subjects one through three, respectively.

The most noticeable feature of the spontaneous activity for Subject 1 (cf. Figure 3-1) is dense activity on channels 27-32. By locating these channels on the vertical axis and then

following to the right, one can observe a cluster of action potentials occurring on many of these channels beginning at 2 seconds. Vertically aligned markers such as these on the raster plot indicate simultaneous activity of multiple neurons, known as bursts. This pattern continues at an average rate of every 12 seconds. Hence, the first Subject did demonstrate periodic bursting, with a period of approximately 12 seconds (0.08 Hz) on channels 27-32. On these channels, few spikes can be observed outside of the bursts, indicating very little activity occurred outside of the bursts. Weaker and shorter bursts were also occasionally observed on channels 33-40, with a frequency below 0.05 Hz. Another notable feature of Figure 3-1 was the activity of channel 22. Spikes can be observed during almost every 2 seconds for much of the recording period. This denotes regular activity observed on channel 22, with spiking at about 0.5 Hz. The rest of channels exhibited sporadic activity.

The spontaneous activity recorded from Subject 2 (cf. Figure 3-2), shows strong activity on channels 49-59 just before 10 seconds, 30 seconds, 50 seconds, etc., approximately every 20 seconds. From this, it is evident that Subject 2 neurons also fired in bursts approximately every 20 seconds (or at a frequency of 0.05 Hz) with little or no activity between bursts. Like channel 22 from Subject 1, channel 36 demonstrated higher frequency activity, around 0.5-1 Hz, evidenced by spikes nearly every 1-2 seconds. Channel 53 behaved uniquely, bursting every 20 seconds in unison with channels 54-59, but also, remaining active between bursts at a frequency of about 0.5-1 Hz. During the spontaneous recording there was only one burst seen on channels 0-35 that occurred during the first 20 seconds of recording.

The data from recording the spontaneous activity of Subject 3 (Figure 3-3) was similar than Subjects 1 and 2. However, in this subject, large bands of high frequency bursting was observed on channels 13-22. Hence, for this data set, the synchronized bursting occurred at a

much higher frequency (1 Hz) than Subjects 1 and 2 (0.05 Hz). Subject 3 also displayed the typical, unsynchronized high-frequency (0.5-1 Hz) active channels (0, 2, 3, 5, 7, 8, 10, 12, 57, 58). The tissue of Subject 3 was significantly more active than all other Subjects. Although there was some evidence of slower bursting (see channels 35-40), activity from Subject 3 could be characterized by more active channels, higher spike frequencies, and even larger amplitude action potentials than other Subjects.

Applied Currents

Data collected with an applied current was filtered and used to create raster plots as well. Patterns of activity during application of each current were in general consistent with those observed during the preceding spontaneous recordings. Raster plots of neural activity during current applications are shown in Figures 3-1B, 3-2B, 3-3B, and 3-3C.

For Subject 1, the pattern of activity during the 10 μ A current (Figure 3-1A) was similar to that observed spontaneously (Figure 3-1B). Unlike the baseline activity, the rate of bursting during the current was slower, decreasing from 0.08 Hz to 0.05 Hz (every 20 seconds). Bursts can be observed on channels 27-32 at 0 seconds, 20 seconds, 40 seconds, and continue with a period of 20 seconds.

Similarly, activity for Subject 2 was comparable in frequency and regularity to baseline recordings (Figure 3-2B). The bursts of activity on channels 47 and above showed periodic bursting during both spontaneous (Figure 3-2A) and current source recordings. During the current source recording several bursts of activity on channels 0-35 were also recorded, though this was observed only once during the initial spontaneous measure (comparison of Figure 3-2A vs. Figure 3-2B for channels 0-35).

The data for Subject 3, shown in Figure 3-3, was unique among the three subjects in that activity occurred at much higher frequencies across more channels than the other two subjects.

During the 5 and 10 μA current source there are a few instances where bursting had occurred, for example, at 75 seconds (Figure 3-3B) and 125 seconds (Figure 3-3C), which is similar to patterns recorded during baseline activity. However, it appears that application of either the 5 or 10 μA current source seemed to slow the rate of activity in terms of the number of channels that were active and the rate of activity on those channels. This slow down is similar to that observed for Subject 1, as described earlier.

Total Spikes Over Time

In order to quantitatively display the amount of activity over the entire dish for each trial, the number of spikes during one-second time bins was collected and plotted. Figure 3-4 shows the rate of activity over time as a histogram obtained from recordings using a 10 $\mu\text{A}/10\text{ Hz}$ applied current on Subject 1 (Figure 3-4A) and Subject 2 (Figure 3-4B). In this histogram, the number of spikes detected on the entire MEA is plotted on the vertical axis and time on the horizontal axis. The time axis is divided into interval bins of 1 second. Hence, each bin represents the total number of spikes detected in a one second interval, essentially smoothing the variability of the rate of activity over time.

For most of the bins for Subject 1, 20-30 total spikes were observed. However, beginning at 1 second and repeating every 20 seconds, the number of total spikes increases sharply to 40 spikes or more. This means that the sum total of the spikes detected with the MEA suddenly increased at a frequency of 0.5 Hz. Similarly, Subject 2 also showed periodicity. For this trial, most of the bins contained 30-40 spikes. Around 10 seconds, a large increase in the number of spikes per bin can be observed, the largest of which contains 75 spikes. Like Subject 1, this sudden increase repeats at intervals of approximately 20 seconds. These histograms reflect the underlying burst events shown in the raster plots described earlier.

Figure 3-5 shows a histogram of spike rate over time for Subject 3 during the 5 $\mu\text{A}/5\text{ Hz}$ (Figure 3-5A) and 10 $\mu\text{A}/10\text{ Hz}$ current (Figure 3-5B). In this subject, bursts were exhibited at much high frequencies with or without the current compared to the other two subjects (near 1 Hz). It follows that histograms created for Subject 3 should display sudden increases in the total number of spikes every second. However, since the bin size is only 1 second, this means that every bar on the histogram corresponds to the location of an expected burst of activity. Hence, all of the bars should be roughly equal in magnitude, without noticeable increases in activity. As expected, the magnitudes of the bars remain relatively constant throughout the trial, with two exceptions at 135 seconds and 170 seconds (Figure 3-5A) and 75 seconds (Figure 3-5B).

Moving Average Filter

The results of the moving average filter were used to display changes in resistance of the ganglion over time. The algorithm was used to calculate moving average results for individual channels, and then to average these results over multiple channels. The moving average trace is simply a graph of resistance or reactance values (vertical axis) shown over time (horizontal axis). A value of zero ohms on the vertical axis of a moving average trace is equivalent to the baseline resistance of the neurons during inactivity. Thus extrema represent temporal locations of sudden shifts in the resistance from baseline. Since such resistance shifts are the main focus of our experiments, these extrema are similarly the main focus of analysis of the moving average traces. Specifically, consistent spatiotemporal correlations of these extrema and spike activity would show evidence of a relationship between these two phenomena.

The resistance using the moving average method is shown in Figures 3-6 through 3-7 during the 10 μA current for Subjects 1 and 2, respectively. The data for Subject 3 under the 5 and 10 μA currents is shown in Figures 3-8 and 3-9, respectively. In each figure, three moving

average traces were produced. Panel A of each figure shows the resistance values calculated by averaging together the moving average traces of all 60 channels of the MEA. Panel B shows resistance values averaged over only a band of active channels (generally channels on which bursting was observed). Panel C of each figure shows values calculated by averaging together the resistance traces of a cluster of inactive channels for comparison. Specifically, the active and inactive traces were qualitatively compared for features such as the number and locations of extrema. A direct subtraction of the two traces proved impractical due to the significantly varying magnitudes of the resistance of the tissue at different spatial locations.

For Subject 1 in Figure 3-6, averaging over all channels during the 10 μ A current resulted in a large resistance peak just before 110 seconds. Twenty seconds later, a series of significant maxima and minima were observed. Large peaks were also observed for Subject 2 and Subject 3 in panel A of Figures 3-7 through 3-9. Analysis over the active channels or inactive channels showed peaks for only one of the three subjects (Subject 3). For subject 1 and Subject 2, there were occasional peaks in the data which were not apparent across each panel. In contrast, Subject 3 shows a clear peak at 95 seconds during the 5 μ A current source and 180 seconds during the 10 μ A current source which appears in each of the three panels. Of the three subjects only the subject which showed the highest rate of activity across the majority of channels showed any consistent change.

Correlating Activity and Resistance

A major function of these experiments was to identify correlations between resistance changes and action potentials in the neural tissue. In order to accomplish this, data from each raster plot and histogram was compared to the corresponding moving average trace. For Subjects 1 and 2, spatiotemporal locations of bursts were compared directly to the resistance traces. First

the bursts were located using the raster plot. These locations were confirmed with comparisons to the histogram, which showed peaks at the temporal location of each burst. Then, the resistance trace at the same instant of time was investigated for maxima and minima. The presence of extrema on the resistance trace of bursting channels occurring simultaneously with the bursts on those channels would indicate a correlation between resistance and activity.

This analysis is shown in Figure 3-10 from Subject 1 and Figure 3-11 for Subject 2. In the figure, vertical line segments are used to designate the location of bursts. Following the segment to the moving average trace from the active channels (Figures 3-10C and 3-11C) allows for observation of the existence of extrema. In the figure, green segments are used to mark bursts in which a simultaneous moving average extremum is present, while red segments are used to designate bursts in which no such correlation could be observed. As both figures show, most bursts did not correspond to an extremum, though a few bursts did show a correlation. The moving average trace was further scrutinized for the presence of observable extrema which did not correspond with a burst. Two such maxima were observed in from Subject 1 (Figure 3-12) at 125 and 175 seconds, and from Subject 2 at 5 and 40 seconds. Each is indicated in the figure by a red circle. For Subject 3, this analysis was also performed, though it is not shown in the figure. Since activity was persistent with a frequency near 1 Hz, such a visual representation would not be practical.

In general, for all trials, strong activity was sometimes accompanied by extrema in the resistance trace, though usually were not. Beginning instead by finding resistance shifts and then comparing to the raster plots and histograms showed similarly mixed results. While some correlations were observed, most moving average extrema were present without a corresponding increase in firing rate or neural activity.

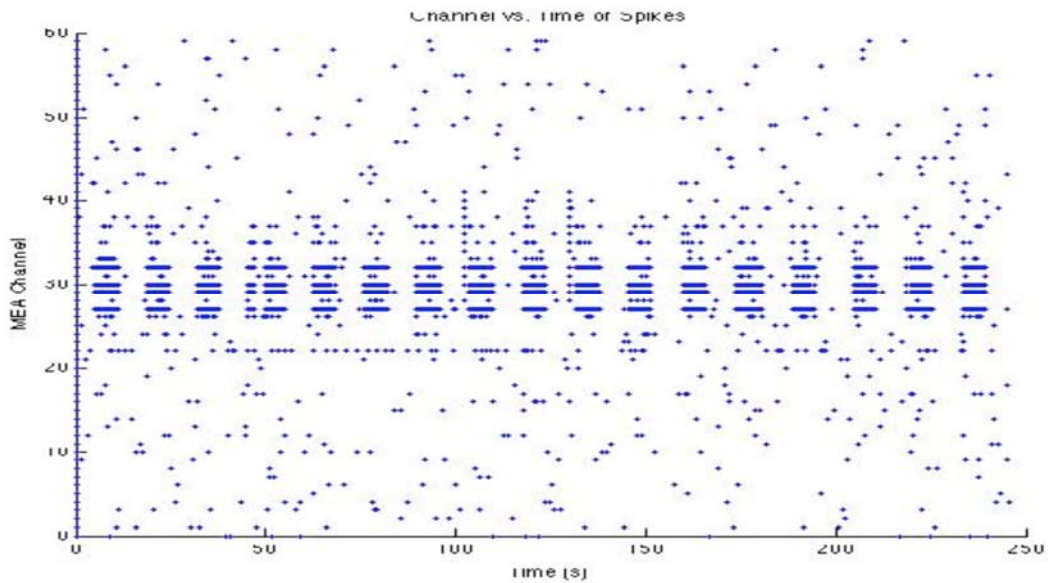
Frequency Analysis

Correlations between resistance shifts and spike activity could also potentially be observed using frequency analyses. The periodicity of neuronal firing in the ganglion cells of each subject has been shown using raster plots and histograms. If a correlation exists between activity and resistance, it may be indicated by corresponding periodic deviations in the resistance trace. For example, bursts were observed in Subject 1 every 20 seconds (0.5 Hz) on channels 27-32. If neural activity can be indicated by resistance changes, then the resistance traces of these channels should also have some component (decrease, increase, minimum, maximum, etc.) which appears every 20 seconds. The presence of such a feature can be isolated using one of several techniques for frequency analysis.

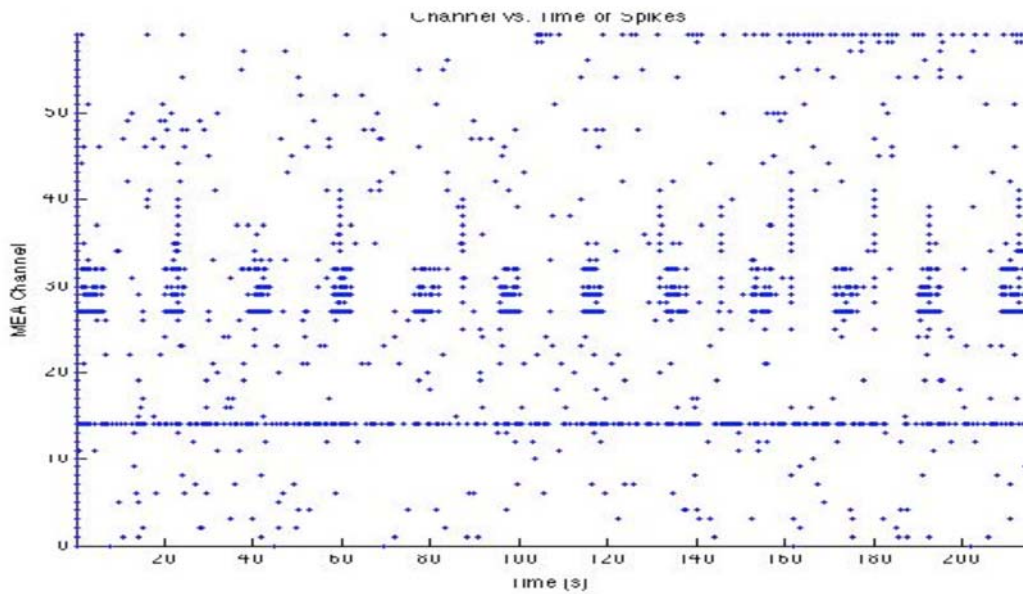
To evaluate frequency dependent factors, a Fourier transform was performed on each moving average trace over clusters of active channels. The Fourier transform was used to convert the data to the frequency domain such that the multiple frequency components of the wave could be directly observed. This resulting data was then displayed on a power spectrum with each frequency value across the horizontal axis and the corresponding power at each frequency on the vertical axis. Prominent frequency components were then compared to the bursting frequencies. Only frequency values between 0 and 1.5 Hz were considered in this analysis since the observed frequencies of bursting activity did not exceed this range.

For Subject 1, bursting was observed with a frequency of 0.05 Hz over channels 27-32. Fourier analysis of the same channels (Figure 3-12) shows a moderately sized peak at this frequency. The strongest frequency component for this trial was observed at 0.5 Hz. Subject 2 exhibited bursting activity at the same frequency. For this subject, two moderately sized peaks are shown around 0.05 Hz (Figure 3-13). However, the graph shows a much stronger component around 0.16 Hz. For Subject 3, periodic firing occurred at frequencies between 0.5-1.0 Hz.

Fourier analysis for each current value (Figure 3-14 and 3-15) shows only small to moderately sized peaks in this frequency range. The largest components observed were at smaller frequencies near 0.2 Hz.

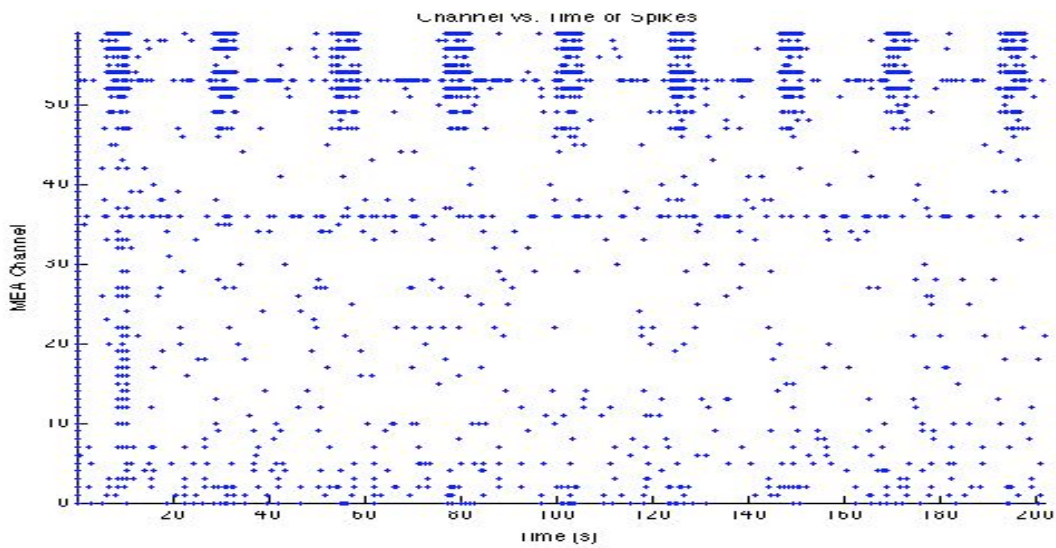


A

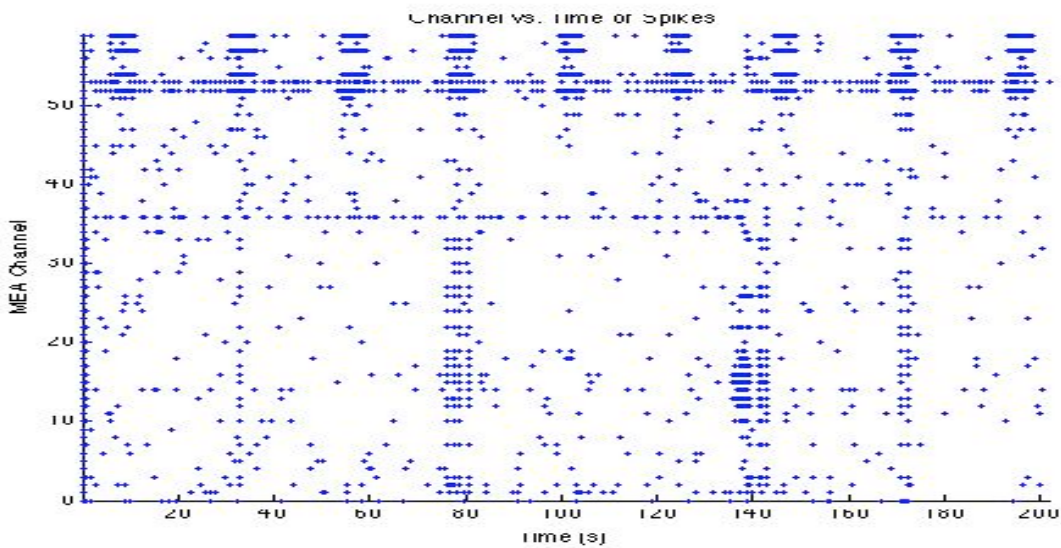


B

Figure 3-1. Raster plots for spontaneous activity of Subject 1 showing the Channel and Time of each spike for A) Baseline activity and B) Application of $10 \mu\text{A}/10 \text{ Hz}$ current. Each blue marker designates a detected action potential. Bursts are identified as simultaneous firings of multiple channels. These can be observed periodically on channels 27-32 with a frequency near 0.1 Hz. During current application, patterns of activity were similar to spontaneous activity observed without the current although bursting frequency did appear to decrease to 0.05 Hz.

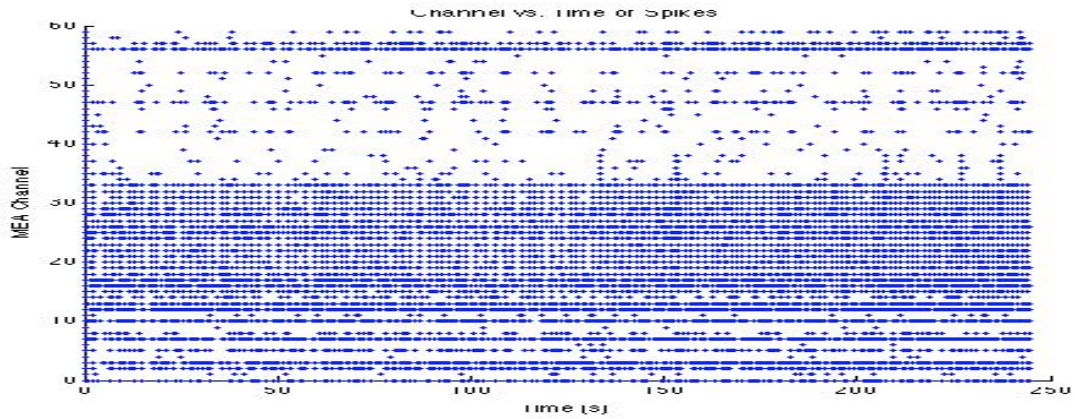


A

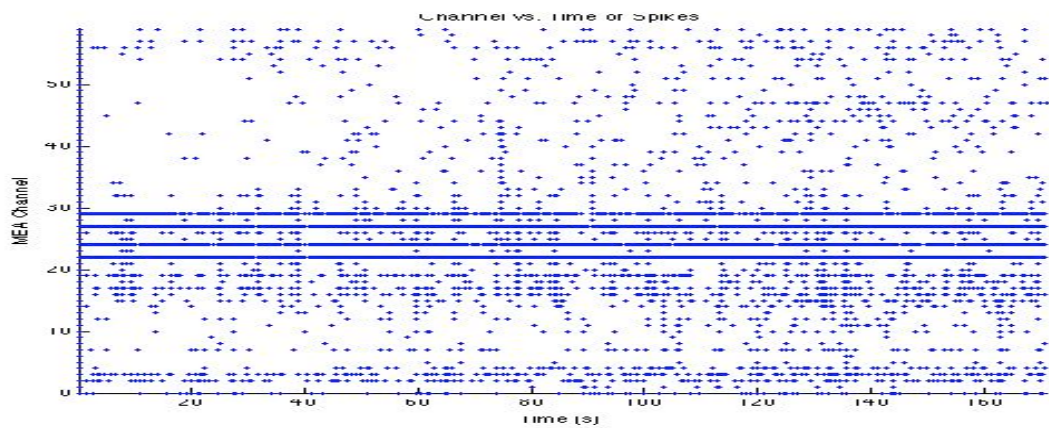


B

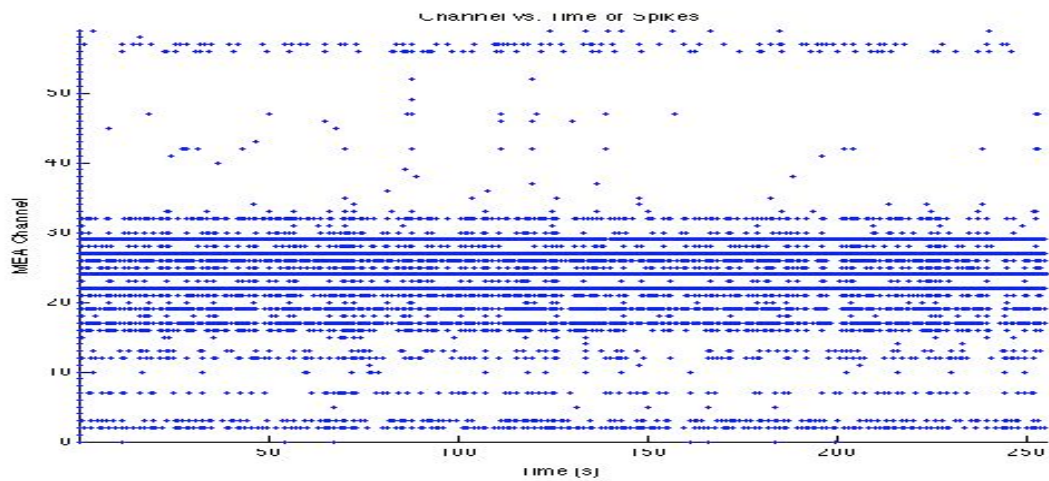
Figure 3-2. Raster plots for Subject 2 during A) baseline activity and B) application of $10 \mu\text{A}/10 \text{ Hz}$ current. Here, bursting can be observed at a frequency of 0.05 Hz on channels 49-59. Channel 36 also exhibits significant spontaneous activity both within and outside each burst. Bursting was still observed on channels 49-59 at a frequency of 0.05 Hz . In this animal there was also evidence of occasional bursts on other channels during the application of the current source (i.e., channels 0-25).



A

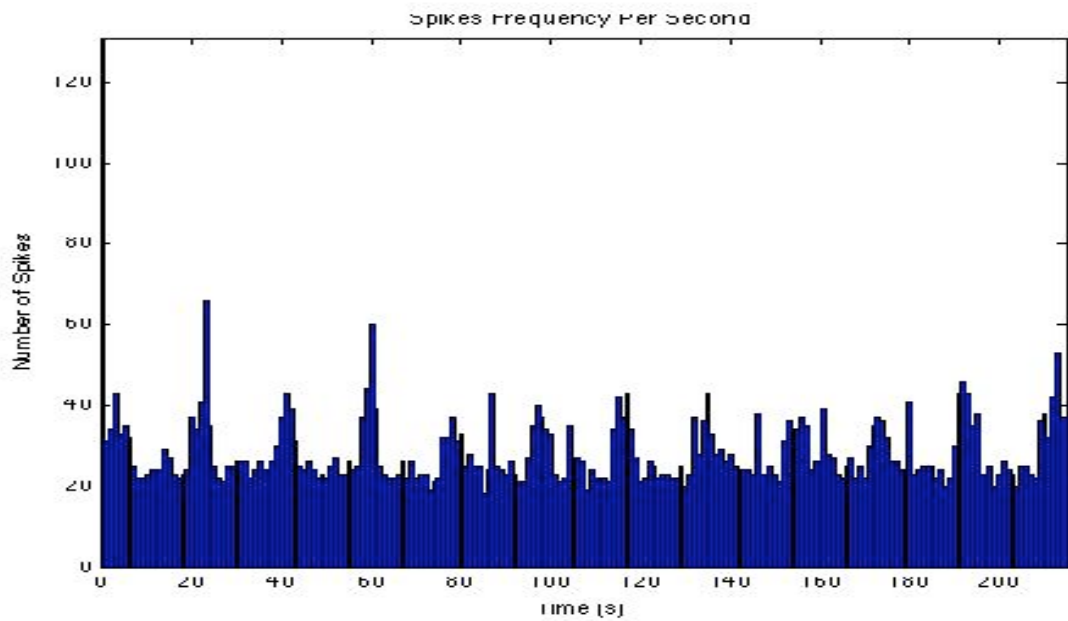


B

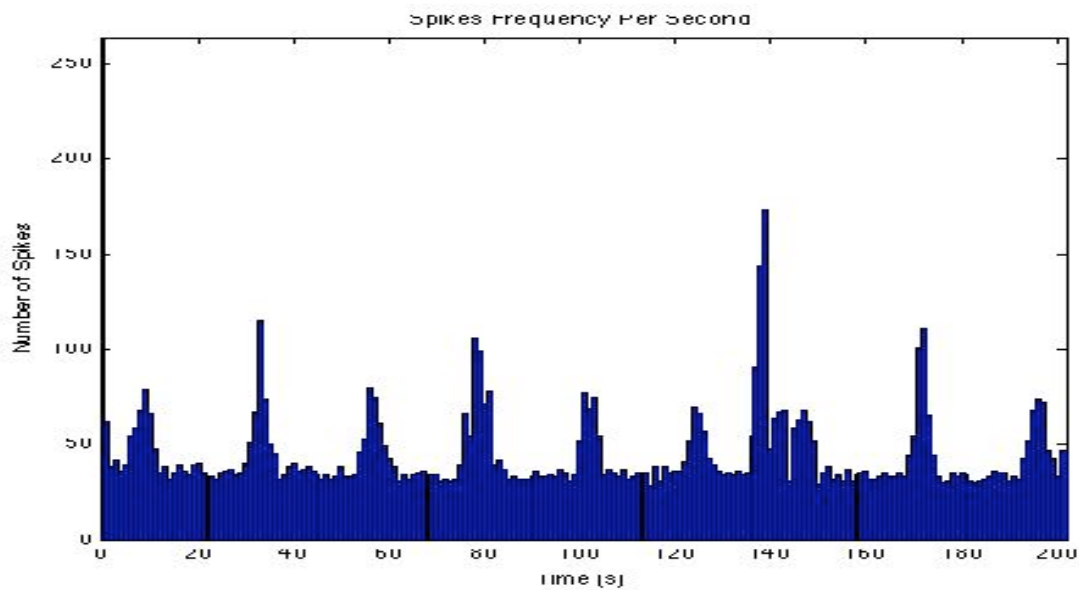


C

Figure 3-3. Raster plot for Subject 3 during A) baseline activity, B) application of 5 $\mu\text{A}/10$ Hz current, and C) 10 $\mu\text{A}/10$ Hz current. This ganglion was extremely active on almost half of the channels, including 1 Hz bursts. Many of the channels between 15-30 remained active near 1 Hz.

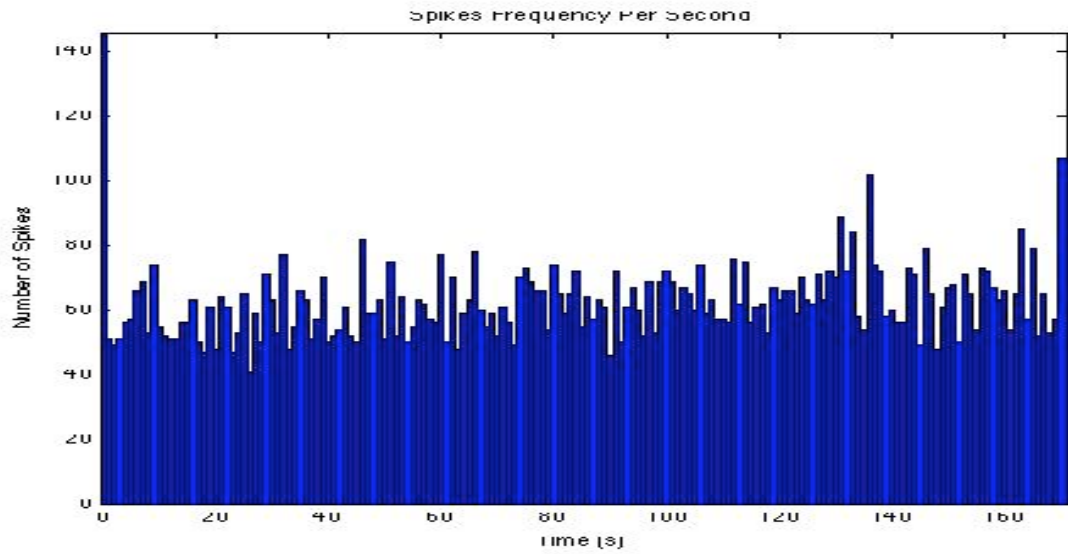


A

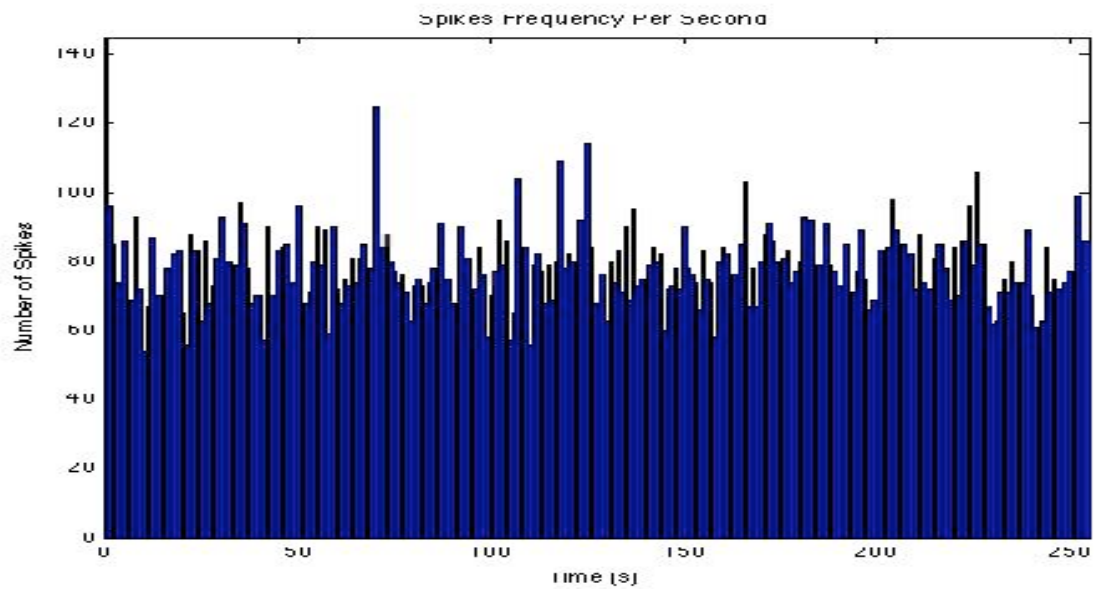


B

Figure 3-4. Spike frequency over time (spikes in each second of data) for A) Subject 1 during application of the $10 \mu\text{A}/10 \text{ Hz}$ current and B) Subject 2 during the $10 \mu\text{A}/10 \text{ Hz}$ current. The almost periodic peaks seen in these figures correspond to the spontaneous bursts that occurred regularly in these animals.



A



B

Figure 3-5. Spike frequency over time (spikes in each second of data) for Subject 3 during A) application of the $5 \mu\text{A}/10 \text{ Hz}$ current and B) the $10 \mu\text{A}/10 \text{ Hz}$ current . For Subject 3, peaks in spike rate are less apparent since activity in this animal consisted almost entirely of rapid spike activity (cf. Figure 3-3 and 3-7).

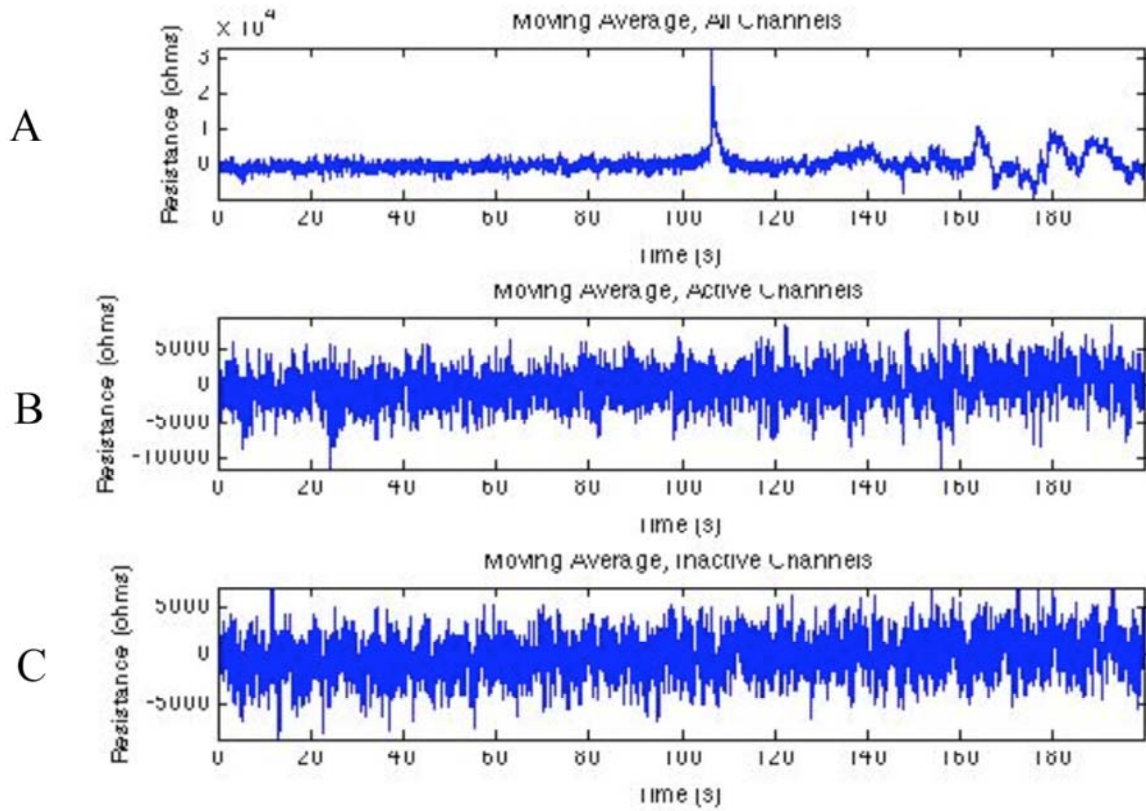


Figure 3-6. Resistance traces from Subject 1 during $10 \mu\text{A}/10 \text{ Hz}$ current calculated for A) all channels, B) active channels, and C) inactive channels. Deviations in the traces indicate shifts in the measured resistance.

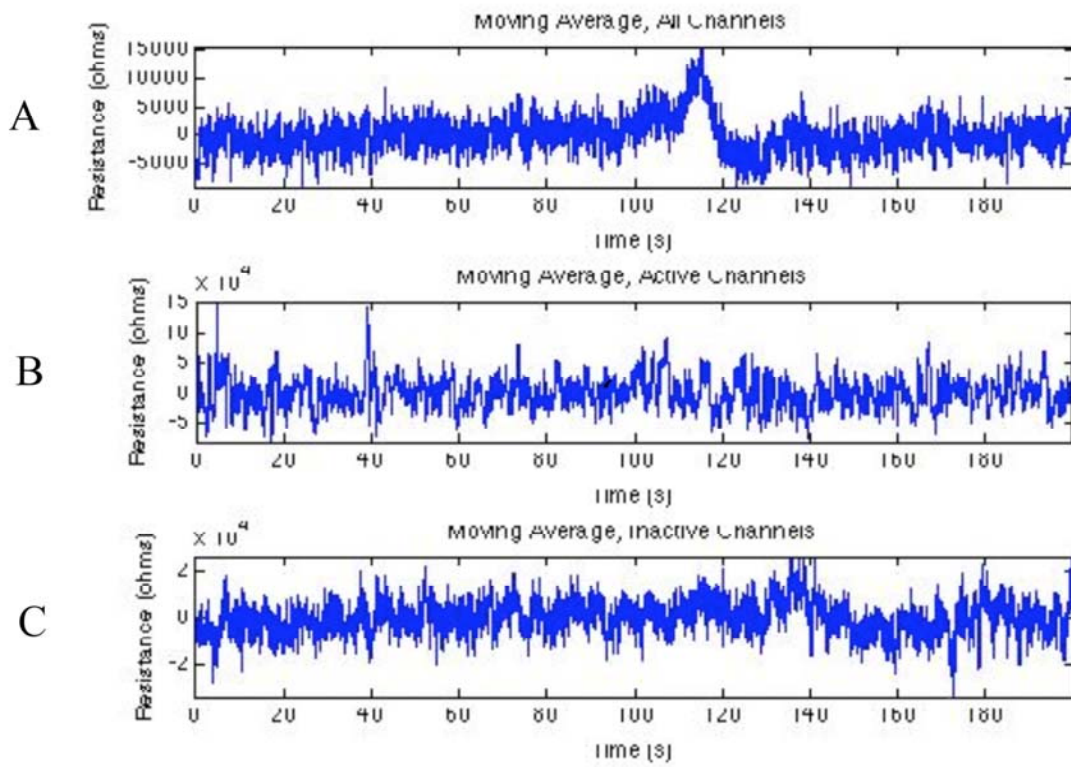


Figure 3-7. Resistance traces from Subject 2 during 10 $\mu\text{A}/10\text{ Hz}$ current calculated for A) all channels, B) active channels, and C) inactive channels.

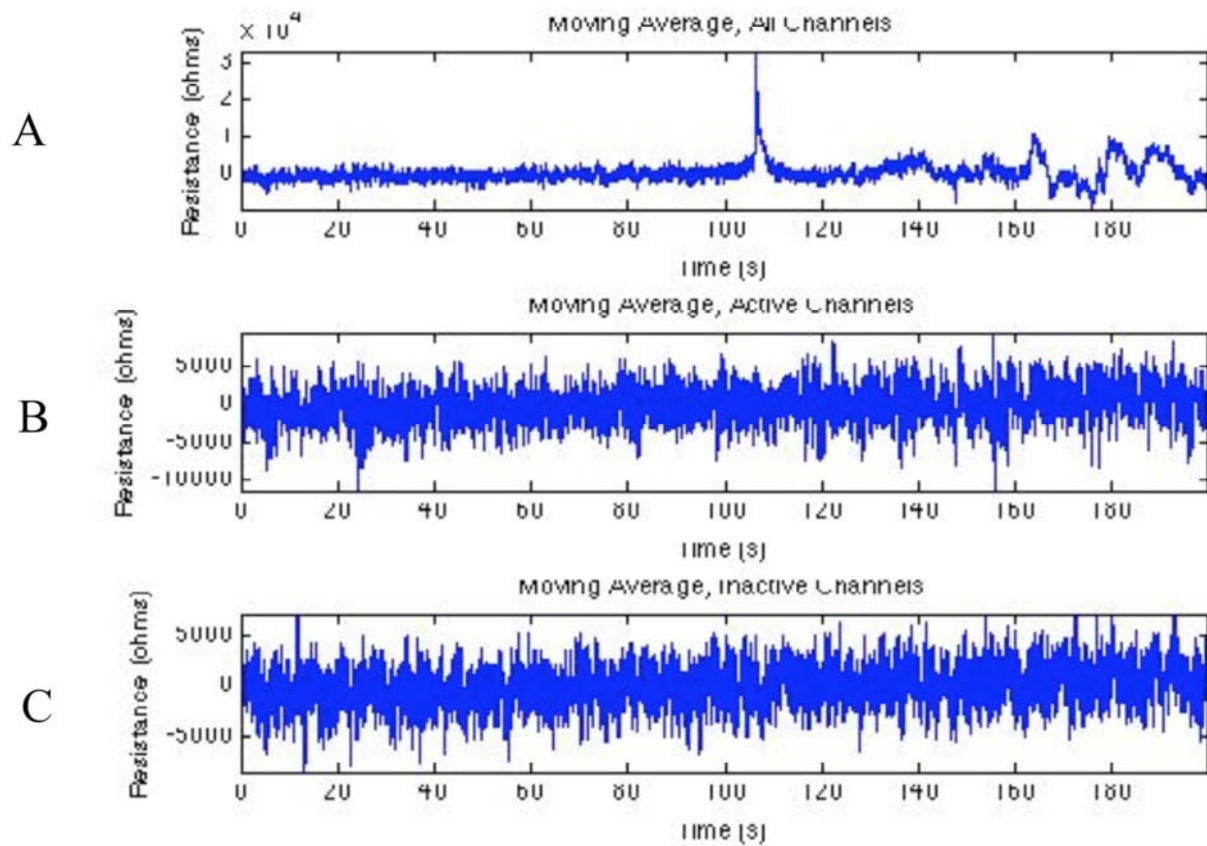


Figure 3-8. Resistance traces from Subject 3 during $5 \mu\text{A}/10 \text{ Hz}$ current calculated for A) all channels, B) active channels, and C) inactive channels. In this animal, a large deviation can be seen at approximately 95 seconds which occurs on all channels, even the channels which had not shown any spontaneous activity in the absence of current.

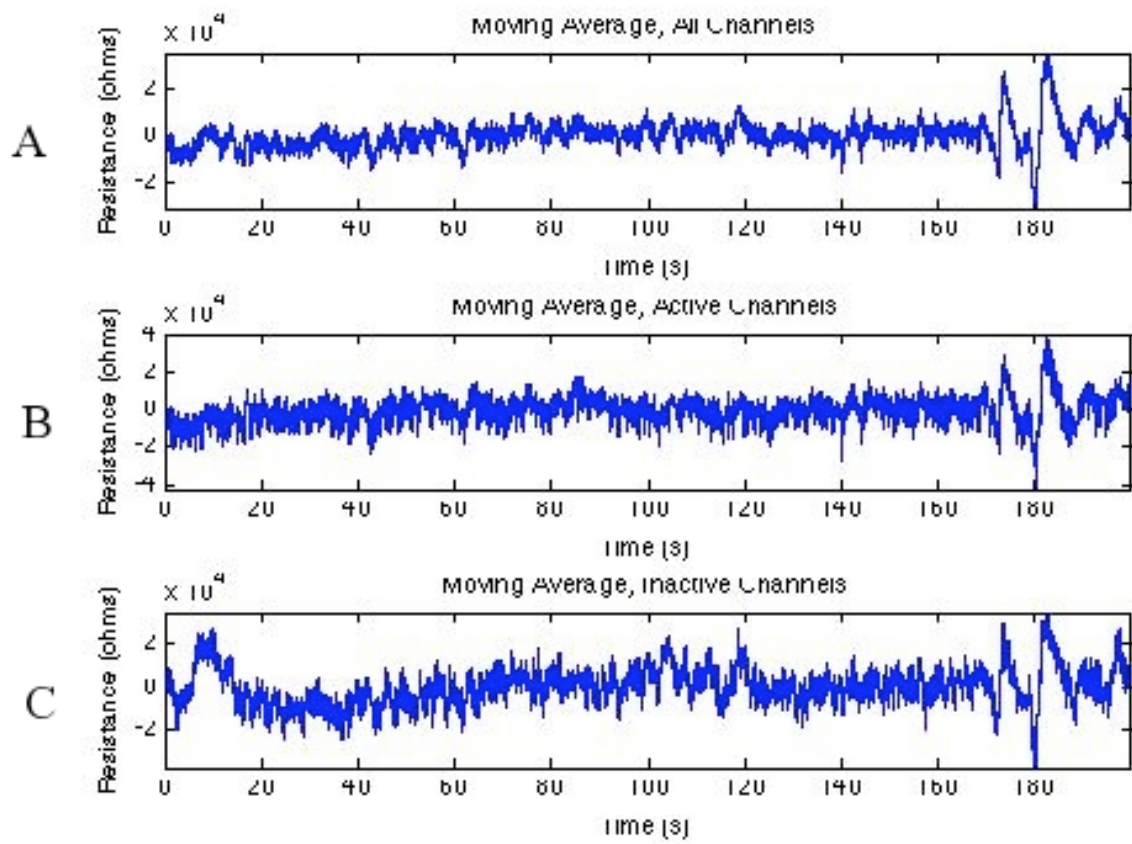


Figure 3-9. Resistance traces from Subject 3 during $10 \mu\text{A}/10 \text{ Hz}$ current calculated for A) all channels, B) active channels, and C) inactive channels.

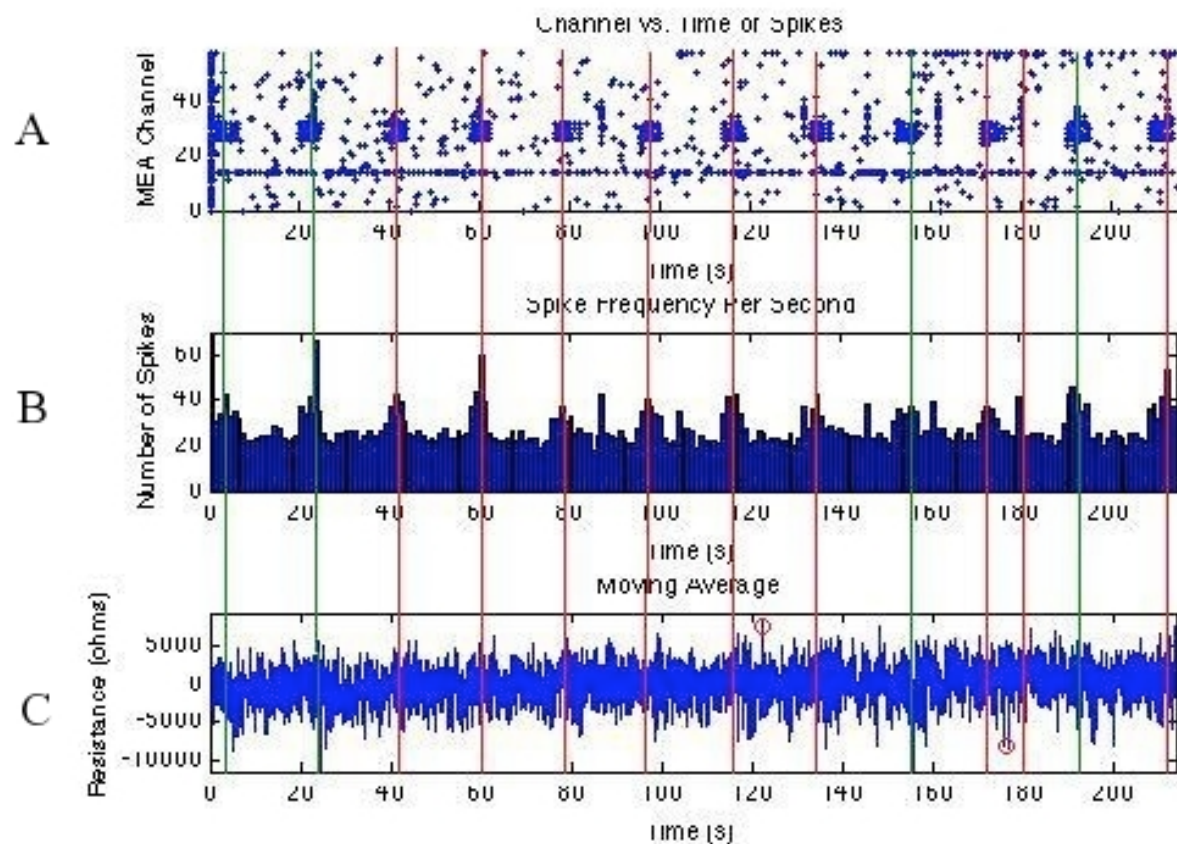


Figure 3-10. Comparative analysis for Subject 1 during application of $10 \mu\text{A}/10 \text{ Hz}$ current between A) raster plot, B) histogram, and C) moving average trace for active channels. Overlaid lines indicate areas of bursting. Green lines designate a possible correlation while red indicate no apparent correlation. Red circles on the panel C indicate two very large maxima which were not simultaneous with bursting.

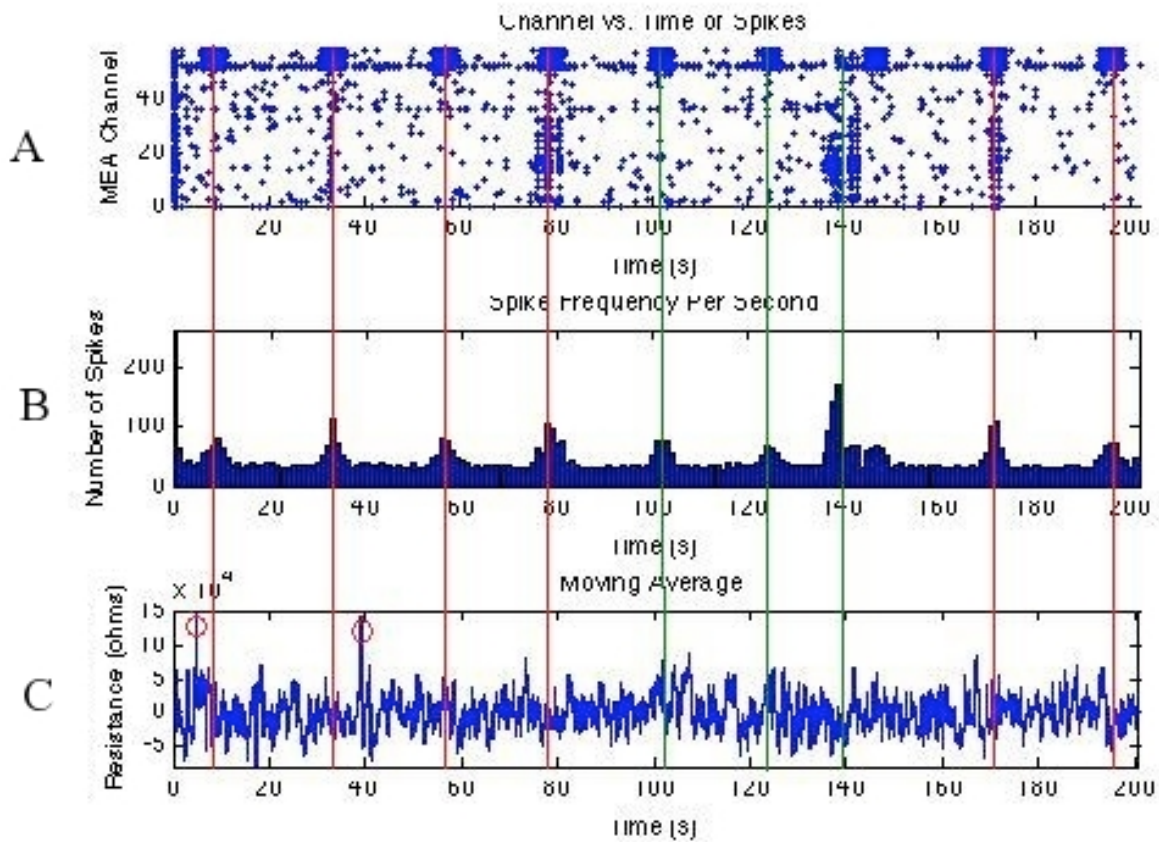


Figure 3-11. Comparative analysis for Subject 2 during application of $10 \mu\text{A}/10 \text{ Hz}$ current between A) raster plot, B) histogram, and C) moving average trace for active channels. Overlaid lines indicate areas of bursting. Green lines designate a possible correlation while red indicate no apparent correlation. Red circles on the bottom panel indicate two very large maxima which were not simultaneous with bursting.

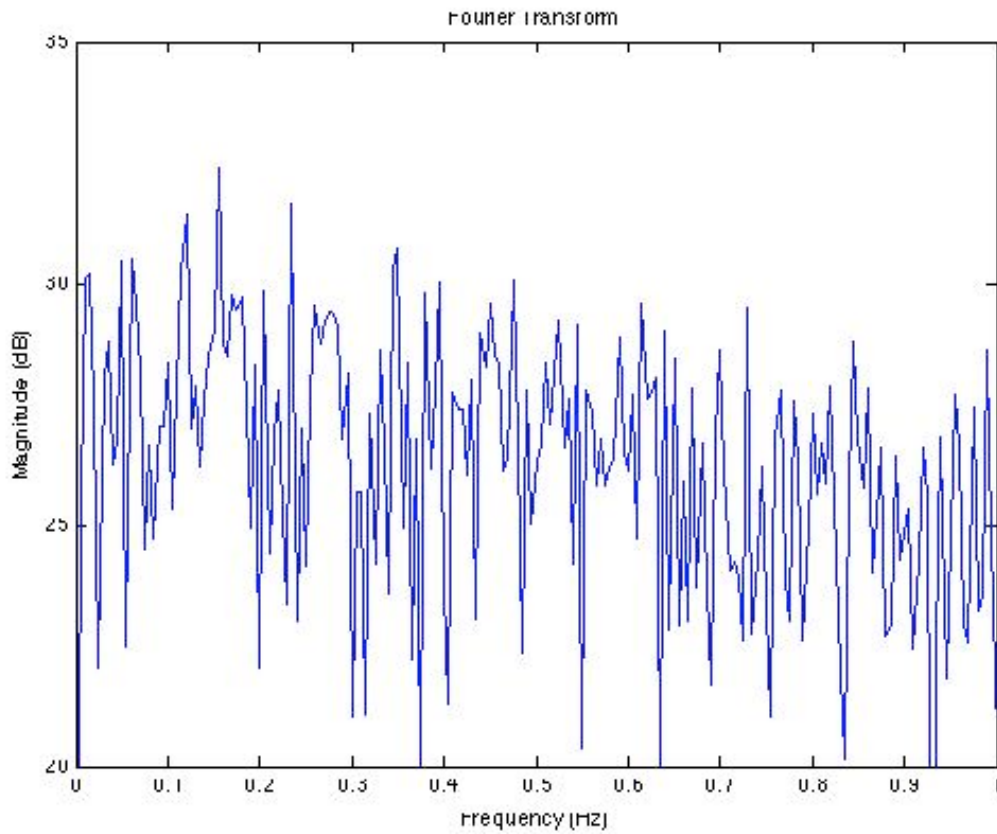


Figure 3-12. Fourier power spectrum of the moving average trace for Subject 1 during application of a 10 μ A/10 Hz current

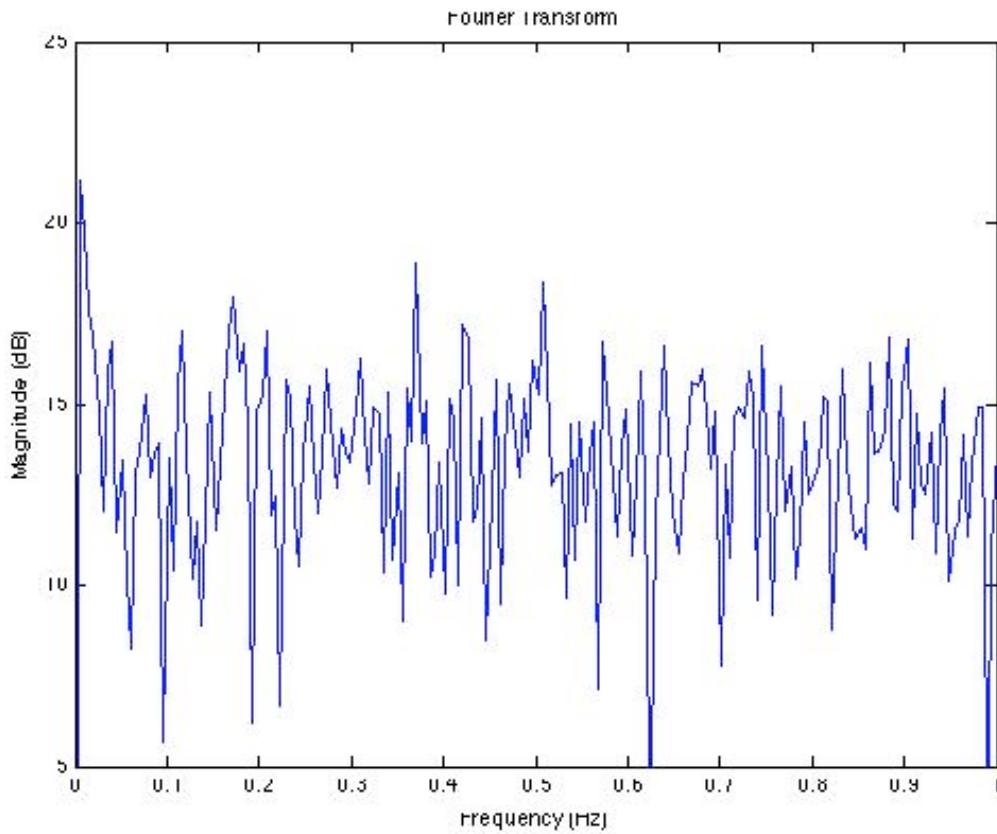


Figure 3-13. Fourier power spectrum of the moving average trace for Subject 2 during application of a 10 μ A/10 Hz current

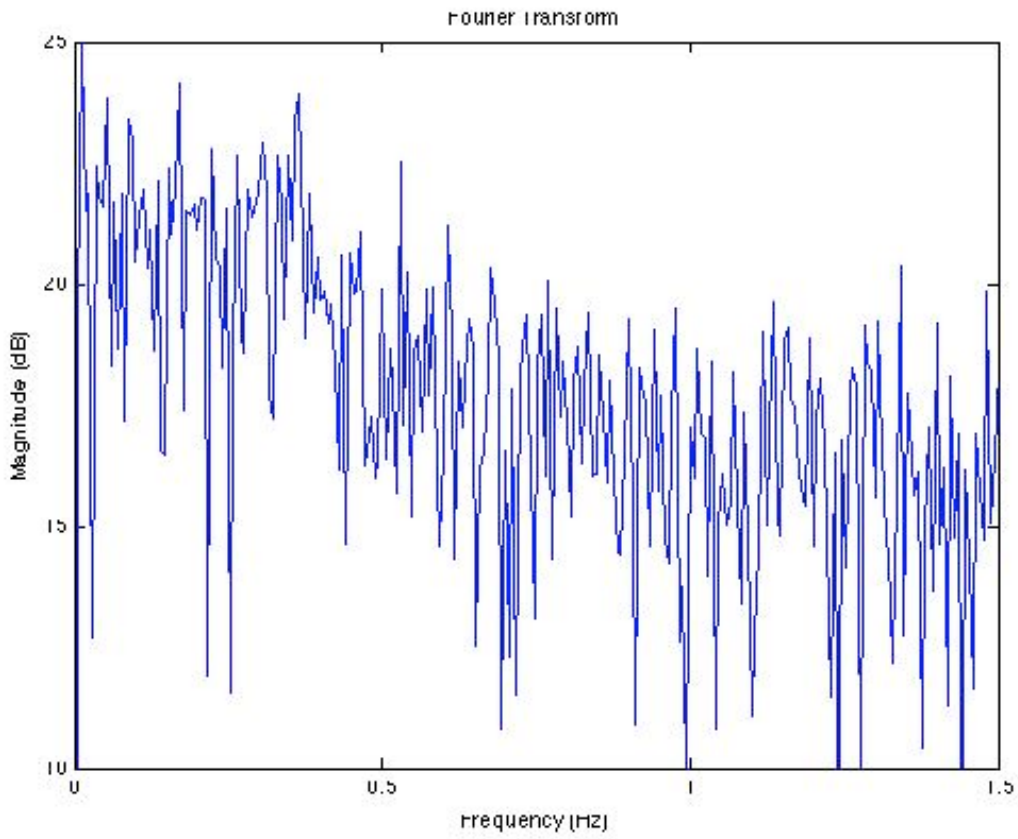


Figure 3-14. Fourier power spectrum of the moving average trace for Subject 3 during application of a $5 \mu\text{A}/5 \text{ Hz}$ current

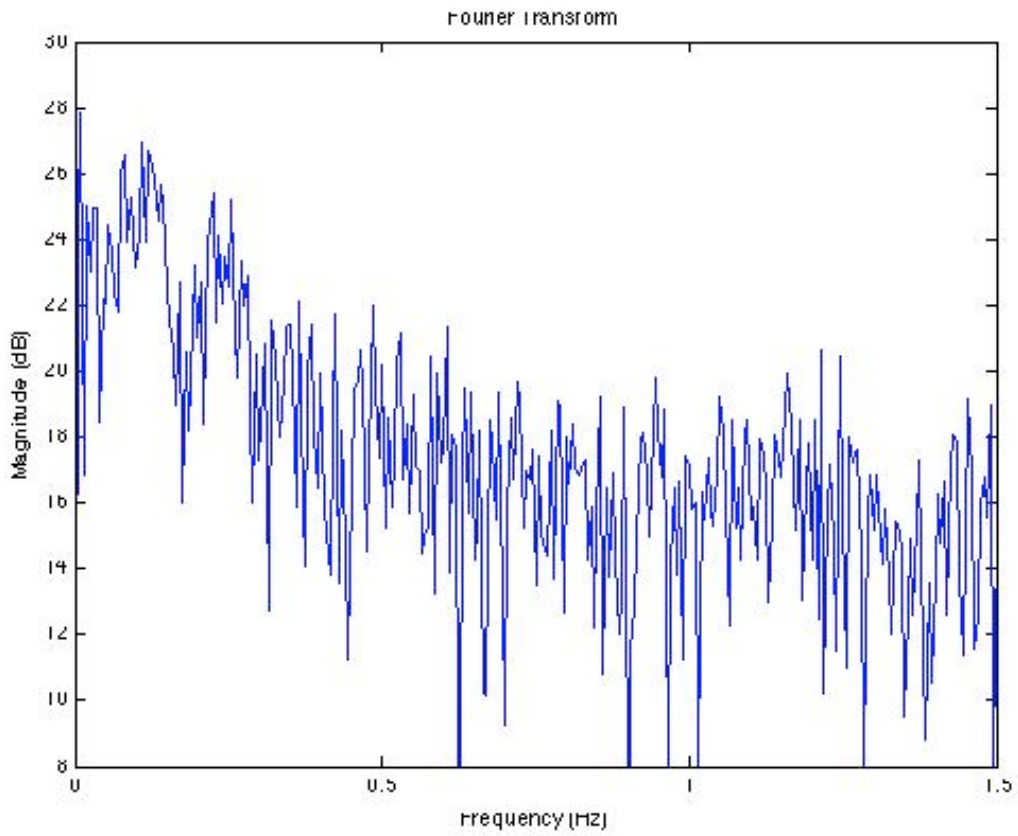


Figure 3-15. Fourier power spectrum of the moving average trace for Subject 3 during application of a 10 μ A/10 Hz current

CHAPTER 4 DISCUSSION

Patterns of Activity and Raster Plots

Using our 64-channel MEA, I was able to successfully record action potentials from the *Aplysia* abdominal ganglion. Moreover, results showed firing patterns which were reasonably consistent with those reported by Novak and Wheeler [64]. However, every type of activity was not observed for every tissue sample used. Instead, slow periodic bursting (0.05-0.08 Hz) was observed in Subjects 1 and 2, while faster bursts (on the order of 1 Hz) were observed in Subject 3. For all trials, activity was generally observed in a cluster of 5-20 adjacent channels for every data set. A few of the remaining channels (fewer than 10) also exhibited activity, each of which was generally unsynchronized with the rest of the channels, and high frequency (~1 Hz). The remaining channels were characterized by sporadic, irregular activity.

The varying patterns of activity observed were likely due to differences in the spatial orientation of the ganglion on the MEA. For each trial, the intention was to position the ganglion such that measurements from the region near R15 would be recorded directly. This proved to be a difficult task as the external features of the ganglion are sometimes not easy to distinguish after dissection, even under a microscope. Based on the previous studies and our results, it is apparent that this placement was successful in Subjects 1 and 2, but not Subject 3. The areas near R15 were those which periodically burst every 10-20 seconds. Though this firing rate is slower than that reported by Novak and Wheeler, this is probably due to variations between animals, each of which demonstrates slightly unique activity patterns. For Subject 3, the rapid firing activity was indicative of poor placement of the ganglion. The 0.5-1 Hz frequency of firing was typical of the white rostral cells, as reported by Novak and Wheeler. However, the bursting observed is in

contradiction with Novak and Wheeler's classification of regular firing. This discrepancy may be explained by a unique step in our methodology. For this subject only, extra care was taken to remove the insulating sheath which surrounds the ganglion cells in order to increase spike amplitude. Since action potentials were so large, they may have been measured effectively enough by distant channels for detection by the spike detector algorithm. Hence, one action potential may have appeared on multiple channels, creating the appearance of bursting activity. This is also significant in explaining the high number of active channels for this Subject. Hence, it is likely that a smaller fraction of the ganglion was firing regularly at 0.5-1 Hz than the results from Subject 3 would indicate.

Applied Currents

Application of a 10 μA current consistently provided the most manageable and useful results as this current value provided efficient and accurate filtration of the sinusoidal current. Even so, changes were noted in the firing patterns of the tissue as compared to spontaneous activity. Specifically, the frequency of bursting in Subject 1 was slower (0.05 Hz) during application of the current versus that observed with no current (0.08 Hz). This decrease in frequency could indicate that the current values used were large enough to affect the behavior of the tissue. Conversely, the changed behavior could be a byproduct of lost data during filtration and spike detection. This latter explanation is also applicable to the sparseness of the raster plots obtained from applied current trials as compared to baseline recordings.

As the 20 and 40 μA currents provided a superior signal to noise ratio in the moving average traces, the relative success of the 10 μA data was unexpected. However, the STG 1008 stimulator which was used to provide the current often created problems in the signal beyond 10 μA . On these trials, artifacts from the stimulator were observed at every transition between one

period of the wave to the next. Every data set using a current higher than 10 μA was marred by this effect. To resolve the problem, these artifacts were later removed from the data set before filtration. However, this process would also remove any action potentials which occurred simultaneously with the artifacts. The artifacts sometimes spanned up to 200 samples, or 0.008 seconds and were removed from every period of the wave, every 0.1 seconds at 10 Hz. Hence, up to 8% of the data was removed in order to eliminate these artifacts. While useful information was still available in the remaining portion of each data set, these recordings were not considered in the final results and analyses here. The 5 and 10 μA data, however, consistently proved useful, could be efficiently filtered, and was devoid of artifacts.

Resistance Changes and Activity

The purpose of the moving average filtration was to quantitatively and visually represent changes in the resistance of the neural tissue over time. Ideally, these deviations would show some consistent relationship to the results of spike detection as represented visually using raster plots. For a single neuron, deviations from this baseline value were expected to show temporal correlation with spiking activity.

Results from the moving average filter from all trials provided modest evidence that resistance changes occur in conjunction with neural activity. Correlations between activity and deviations in the moving average trace were successfully found, though not consistently. Qualitatively, changes in the shape of the moving average trace appeared similarly random, with little dependence on activity. Traces from active channels and inactive channels were hardly distinguishable in Subject 1, both remaining reasonably flat with only a few small extrema. In contrast, the active and inactive traces calculated for Subject 2 showed little correlation to one another. For Subject 3 at both current amplitudes, active and inactive channels showed

deviations away from baseline, sometimes correlating together and sometimes not. Hence, it could not be concluded that the presence of maxima and minima in each trace was dependent on the amount of activity present on the channel from which the trace was calculated.

Another method used to isolate relationships between activity and resistance was the comparison of histogram data to the resistance traces. The histograms were useful as a second means by which to visualize instances of high neural activity in addition to raster plots. The resistance traces obtained over all of the active channels of a trial were compared to the sum total activity of these channels over time. Instances at which the amount of spikes in a second over the whole dish drastically increased should create a change in the resistance of all of the active channels, which would be apparent in the resistance trace. Lining up the time axes of the histograms with their corresponding resistance traces and comparing showed the same results as comparisons to the raster plots. Correlations existed, though not on a consistent basis. This is especially obvious using data from Subjects 1 and 2. In these data sets, the histograms show sharp increases in activity which correspond to the bursting of the R15 region of the ganglion once every 20 seconds. In contrast, the active channel resistance traces for these trials remained rather flat. Further, what extrema were present did not visibly show any correlating periodicity. Large peaks present on the moving average trace of Subject 1 at 125 and 175 seconds were not accompanied by a burst. Large peaks observed in Subject 2 at 5 and 40 seconds come too early and too late, respectively, to correlate with observed bursts. For Subject 3 at both current levels, the result is reversed; the histogram is relatively flat due to the constant firing of the cells, though extrema were present in the resistance traces. Hence, a consistent relationship between histogram data and the resistance traces also could not be confirmed.

Frequency and periodicity were also an indicator as to whether correlations existed between resistance changes and neural activity. If neural activity is truly characterized by changes in neuronal resistance, then the resistance traces should show periodic character with the frequency of the associated periodic neuronal activity. For Subjects 1 and 2, active channels burst with a frequency of 0.05 Hz, or every 20 seconds during application of current. Hence, if a correlation does exist between activity and resistance changes, moving average traces on these channels should display periodic deviations with a period of 20 seconds. Similarly, for Subject 3, the spike frequency of 1 Hz should correspond with deviations in the resistance trace.

Fourier transforms were used to help affirm the absence of correlations between frequency and activity. For Subject 1 and 2, a peak was expected at or near 0.05 Hz on the Fourier power spectrum. For Subject 3, a prominent peak was expected at 1 Hz. For each trial, peaks expected on the Fourier power spectrum sometimes existed, but were never prominent. The very presence of peaks at the expected frequencies may provide some possible indication of the correct periodicity, but the results remain inconclusive due to the weakness of the amplitude.

It should be noted that any high frequency components were lost during the moving average process. Because the moving average window is 0.1 seconds wide, equivalent to one period of the 10 Hz sinusoidal current, the average magnitude of the current within one window is always zero. Moreover, any waveform with a frequency that is a multiple of 10 Hz, such as 60 Hz, will similarly have an average magnitude of zero. Hence, these components were cancelled out of the frequency band. Furthermore, calculation of the response characteristics of the moving average filter showed that the gain of the filter decreases with increasing frequency for values which are not multiples of 10 Hz. At high frequencies, on the order of kHz, the gain of the filter drops to less than 0.003. Thus, components at these frequencies, such as action potentials (which

have a duration of approximately 1 ms, equivalent to 1 kHz), are significantly attenuated.

Because of this, action potentials themselves do not influence the values of the moving average trace. Instead, only the indirect effect of the action potentials on the resistance should be manifested in the trace.

To corroborate all of this evidence, a moving average trace was created for an individual channel, 36 from Subject 2 using a 10 μA current (Figure 4-1). This channel showed unique behavior as evidenced by the associated raster plot for this data set (Figure 4-2). The distinguishing feature of this channel was that it was active for the first 150 seconds of recording, but then becomes noticeably less active in the last 50 seconds. Hence, if a correlation exists, the moving average trace should show some type of change in its behavior for 150 seconds, and then transition to a different type of behavior in the final portion of the recording. Results from the moving average trace in the figure showed no such transition. Channel 4 of the 5 μA recording of Subject 3 was also inactive and then active for long, separate stretches of the trial. Like channel 36 in Subject 2, no distinct transition in the resistance trace corresponded to the activity measured on the channel.

While it is apparent that deviations in the moving average trace showed only little correlation to activity in the neurons, the question remains as to where these deviations originate. The answer is likely due to random conditions which alter the initial MEA recording. While watching the data move across the oscilloscope software during recordings, the signal can be observed deviating away from its properly centered alignment. The most obvious example of this is random noise. However, noise would doubtfully create deviations on the scale of those seen in some of the moving average traces.

Poor contact between the ganglion tissue and the MEA could lead to erroneous data. One of the most difficult aspects of the setup of these experiments was the placement of the neural tissue on the MEA dish. Even with the use of PEI, the tissue often adheres poorly to the dish. Hence, during recordings, the tissue may have been partially floating in the ASW, allowing the tissue to move in the dish during recordings. In this situation, the movement of the tissue may not have significantly affected action potential recordings, but may have had a drastic effect on the moving average calculations.

Wherever they originate from, there is some evidence that deviations occurring during recordings corrupt the moving average data. Referring back to Subject 1, the resistance trace across all channels displayed a very large peak just before 110 seconds, and a number of other extrema thereafter. However, the traces from the active channels and the inactive channels do not show these extrema and, in fact, are relatively flat. Review of the original raw data showed that channels 58 and 59 began to visibly drift during the initial peak before 110 seconds, and continued to drift through the remainder of the data set (Figure 4-3). Figure 4-4 shows resistance traces of channels 58-59, and the average of channels 0-57, and the overall average across all channels. Panel A (all channels) and panel C (channels 58-59) are quite similar, both showing deviations which temporally correspond to the drifting. Once the drifting channels (58-59) were removed and the average was recalculated across the rest of the channels (0-57), the large peaks disappeared (Figure 4-4C).

This finding leads to two conclusions. First, deviations in the initial recordings caused by external factors can have significant effects on the end results and analysis. Second, though multiple channels were averaged together, one or two corrupt channels can have drastic effects on the overall averages. The large problem, however, is not these drifting channels. Channels

like 58 and 59 in Subject 1 are obviously corrupt and can be removed from the moving average calculation. Instead, lower magnitude drifting is not so easy to identify and remove. This could be the cause of some of the observed extrema in the resistance traces, and a difficult obstacle to avoid in future work.

Another example of this behavior occurred in the results from Subject 2. In Figure 3-6, moving average traces were shown for this data set, including averages over the active channels (54-59). However, activity was actually observed on channels 51-59, though channels 51-53 were removed from the collection due to significant drifting. Figure 4-5 shows the original trace from Channels 54-59, and the new trace, calculated over channels 51-59. The new trace is much different, now exhibiting a peak at 115 seconds. Hence, while the specific set of channels used to calculate resistance traces exerts an impact on the shape and characteristics of the trace, the amount of activity on the channels chosen is not the causal variable. Moreover, the new trace proves that channels 51-53 are large contributors to the overall shape of the trace calculated over all channels, showing helping to further affirm that drifting channels cause large deviations in the resistance trace.

Microelectrode Arrays and Future Work

Data collection using a 64-channel 3-D MEA proved successful in obtaining spatiotemporal information about neuron spiking activity. Action potentials were clearly visible to the human observer, and easily detected using MEABench OSX software. Furthermore, patterns of activity observed using these MEAs were consistent with those reported in past literature. However, some obstacles existed in using this modality for identifying changes in resistance. There appear to be problems within the experimental setup that would have to be corrected in order to use MEAs as a viable means for measuring such resistance changes. Care must be taken to prevent any perturbations in the system which could affect data acquisition.

Most importantly, it is essential that strong contact is made and maintained between the tissue and the MEA for the duration of all recordings.

Aside from externally driven shifts in the moving average trace, even those shifts that were apparently real were difficult to analyze. Local extrema were successfully observed in each trial. However, the small magnitudes of some maxima and minima left doubt as to whether these were true extrema or merely the results of noise and random fluctuations. This could be remedied with an improved signal to noise ratio. Unfortunately, the stimulator produced artifacts during application of currents larger than $10\ \mu\text{A}$. If this problem can be solved, the signal to noise ratio can be improved, which would increase the size of observable changes in resistance. The resistance is calculated by dividing the voltage by the current as defined by Ohm's Law. Specifically, the moving average trace is calculated for the voltages recorded by the MEA and then divided by the magnitude of the injected current to obtain the resistance. Hence, increasing the magnitude of the current will cause a proportional increase in the recorded voltages for a given value of the resistance. Thus, small deviations caused by noise, perturbation, movement, etc. may prove insignificant relative to the large magnitude of the voltage changes (and thus, the resistance changes). Further, though large voltages would overwhelm the action potentials, spike detection will be unaffected since the sinusoidal current is filtered out of the signal first. Significant improvement may require currents even larger than $40\ \mu\text{A}$, which would stimulate the tissue. Though I have studied only spontaneous activity here, stimulation may prove more useful. Indeed, considering the randomness of the results observed here, the predictability and control gained with evoked activity may prove superior.

Functional Magnetic Resonance Electrical Impedance Tomography

A new technique, called functional magnetic resonance electrical resistance tomography (fMREIT), would be a promising new method for imaging neural activity *in vivo*. This method uses an MRI scanner to collect maps of the magnetic flux density within the tissue, a result of the flow of electric current. Hence, this data reflects changes in resistance. During neuronal activity, the increase in the flow of current into the intracellular space will be apparent using an fMREIT scan due to the accompanying change in conductivity of the cell membrane. Thus, by imaging the changes in resistance, the scan is indirectly imaging neural activity. Most importantly, if successful, this technique would image neural activity with the spatial resolution of an MRI, but with improved temporal resolution [66].

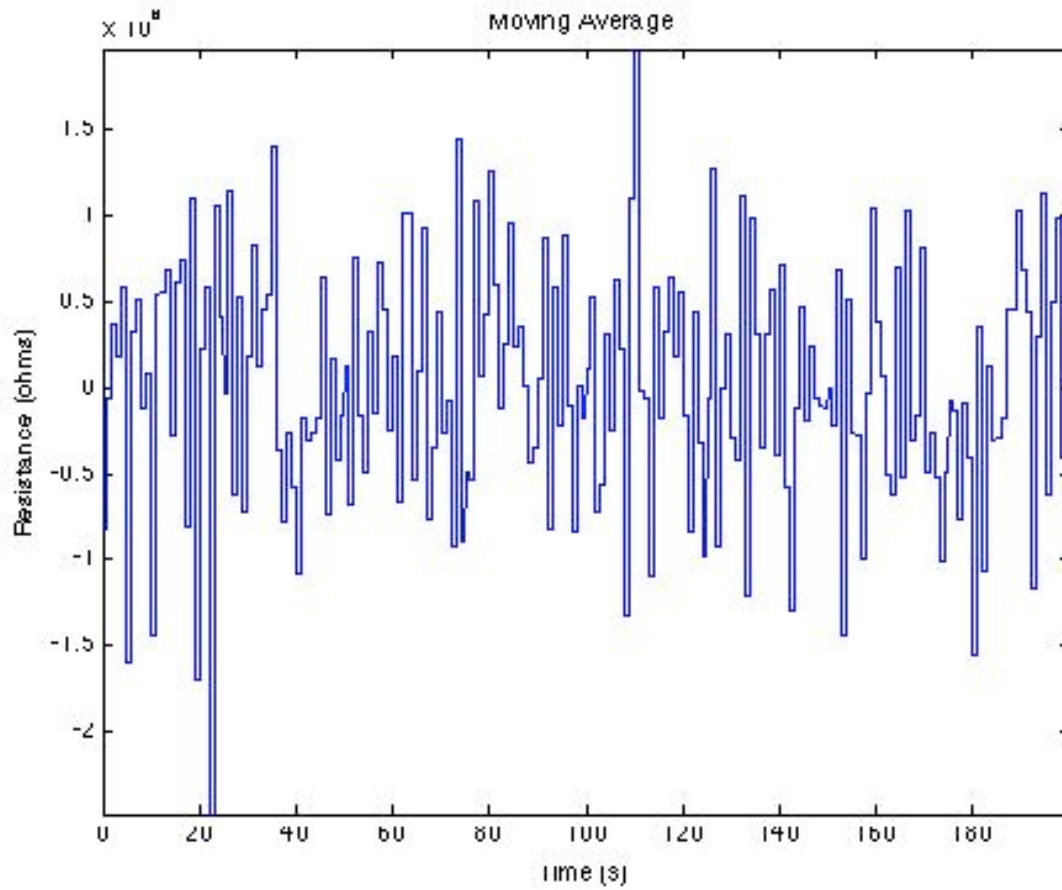


Figure 4-1. Moving average trace for Channel 36 of Subject 2 during application of $10 \mu\text{A}/10$ Hz current. This channel was active for the first 150 seconds of the recording, and then inactive.

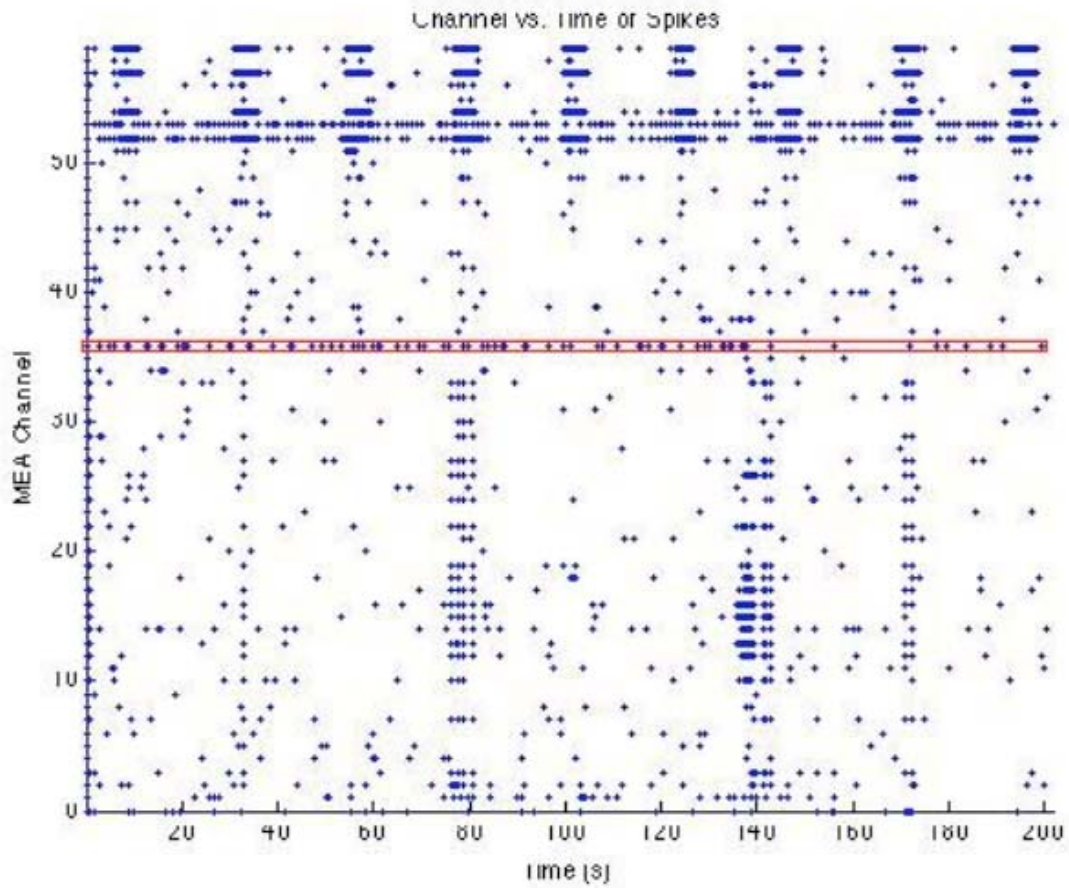


Figure 4-2. Raster plot for Subject 2 during application of 10 μ A/10 Hz current. Channel 36 (indicated by a red box) is active for the first 150 seconds and then becomes relatively inactive.

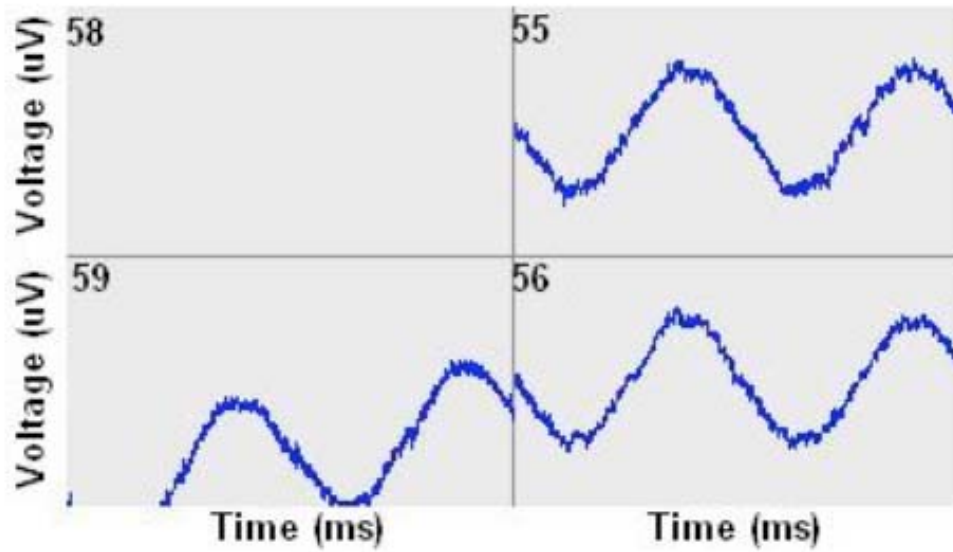


Figure 4-3. Image of four channels from the oscilloscope during Subject 1 recordings with current. Channel number is indicated in the top left corner of each window. The two channels on the left side, 58 and 59, began to drift while the other channels remained stable.

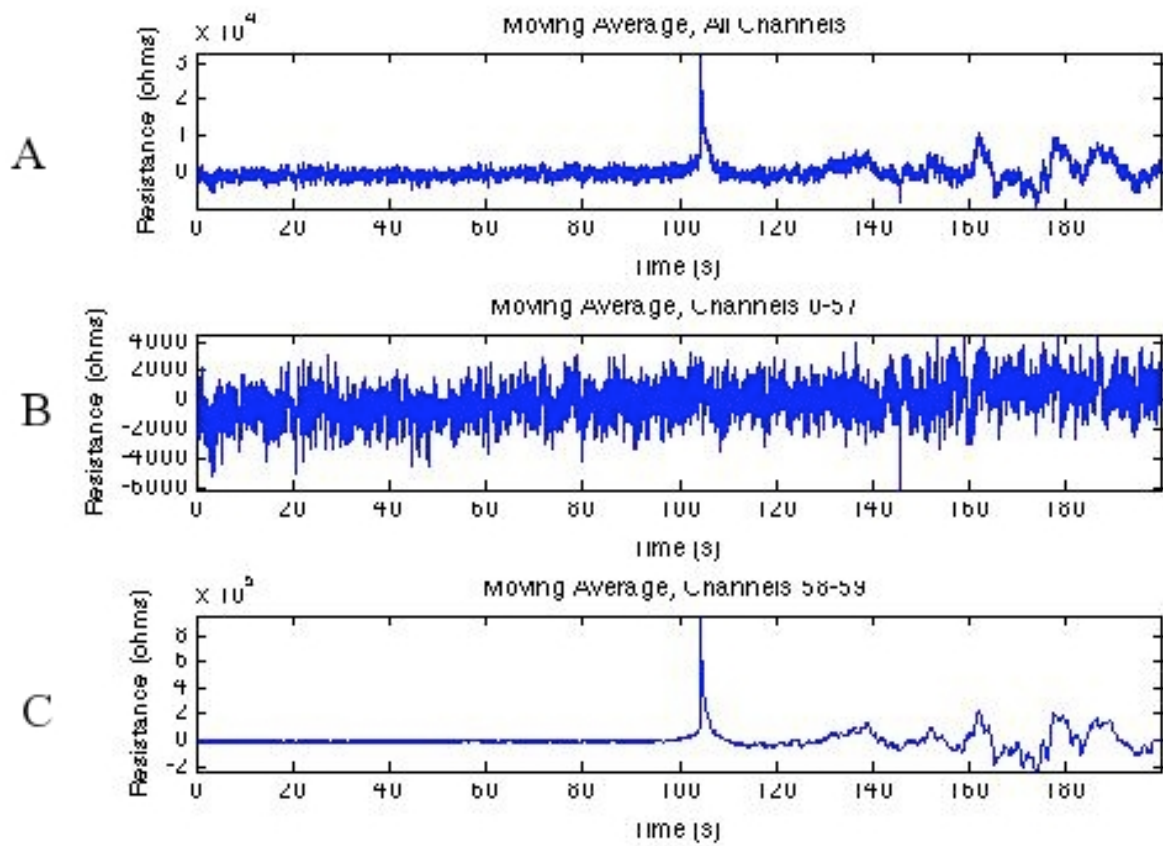


Figure 4-4. Resistance traces for Subject 1 during application of current for A) all channels, B) channels 0-57, and C) only channels 58-59.

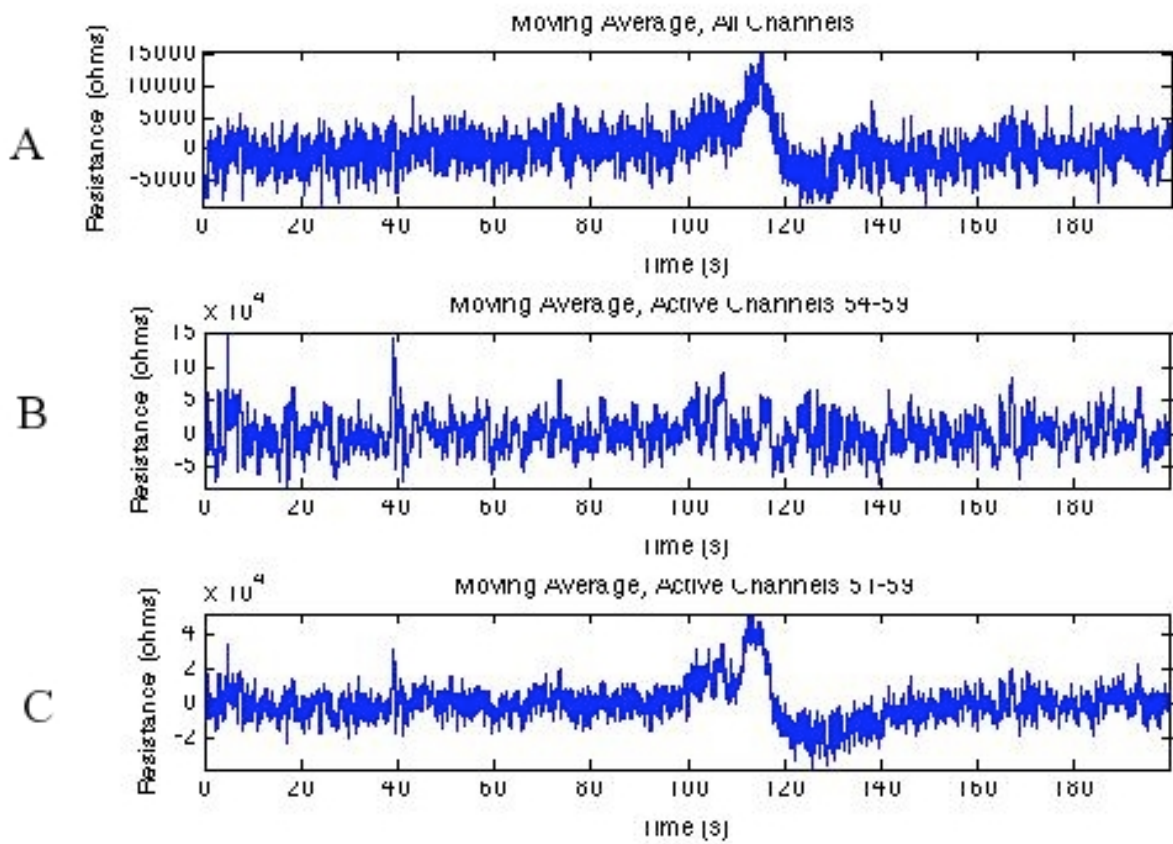


Figure 4-5. Resistance traces for Subject 2 during application of current for A) all channels, B) active channels 54-59, and C) active channels 51-59.

CHAPTER 5 CONCLUSION

The results obtained in the experiments described have shown that MEAs are well suited for recording the spatiotemporal characteristics of neural activity from *Aplysia* abdominal ganglion. Unfortunately, the results could not be used to confirm a consistent relationship between resistance changes and activity in neural tissue, whether that neural activity is always accompanied by resistance changes, or vice versa. This relationship has been observed and reported in previous literature. Trouble in the experimental setup and analysis techniques caused the inability to prove the desired relationship. Poor signal to noise ratios led to difficulty in identifying resistance changes. Under these conditions, the results may have been susceptible to external factors which created corrupted results. The results here also have not led to a conclusion that a relationship between resistance changes and activity in neural tissue absolutely do not exist. With the proper improvements to the experimental setup, the topic still merits further exploration

LIST OF REFERENCES

- [1] M. Pascual, E. Pozas, M. J. Barallobre, M. Tessier-Lavigne, and E. Soriano, "Coordinated functions of Netrin-1 and Class 3 Semaphorins in the guidance of reciprocal septohippocampal connections," *Molecular and Cellular Neuroscience*, vol. 26, pp. 24-33, 2003.
- [2] E. Stein and M. Tessier-Lavigne, "Hierarchical organization of guidance receptors: silencing of Netrin attraction by Slit through a Robo/DCC receptor complex," *Science*, vol. 291, pp. 1928-1939, 2001.
- [3] A. C. Yu, E. Hertz, and L. Hertz, "Alterations in uptake and release rates for GABA, glutamate, and glutamine during biochemical maturation of highly purified cultures of cerebral cortical neurons, a GABAergic preparation," *J. Neurochem*, vol. 42, pp. 951-960, 1984.
- [4] R. Albin, A. Young, and J. Penney, "The functional anatomy of basal ganglia disorders," *Trends Neurosci*, vol. 12, pp. 366-75, 1989.
- [5] A. Nobin and A. Bjorklund, "Topography of the monoamine neuron systems in the human brain as revealed in fetuses," *Acta Physiologica Scand Suppl.*, vol. 388, pp. 1-40, 1973.
- [6] P. Somogyi, A. J. Hodgson, and A. D. Smith, "An approach to tracing neuron networks in the cerebral cortex and basal ganglia. Combination of Golgi staining, retrograde transport of horseradish peroxidase and anterograde degeneration of synaptic boutons in the same material," *Neuroscience*, vol. 4, pp. 1805-1852, 1979.
- [7] A. C. Guyton and J. E. Hall, *Textbook of Medical Physiology*, vol. 11. Atlanta, Georgia: W.B. Saunders Co, 2005.
- [8] G. Buzsaki, *Rhythms of the Brain*. USA: Oxford University Press, 2006.
- [9] C. Croona, M. Kihlgren, S. Lundberg, O. Eeg-Olofsson, and K. E. Eeg-Olofsson, "Neuropsychological findings in children with benign childhood epilepsy with centrotemporal spikes," *Developmental Medicine and Child Neurology*, vol. 41, pp. 813-818, 1999.
- [10] M. Modarreszadeh and R. N. Schmidt, "Wireless, 32-channel, EEG and epilepsy monitoring system," presented at 19th Annual International Conference of the IEEE, Chicago, IL, USA, 1997.

- [11] J. D. R. Millan, F. Renkens, J. Mourino, and W. Gerstner, "Noninvasive brain-actuated control of a mobile robot by human EEG," *IEEE Trans Biomed Eng*, vol. 51, pp. 1026-1033, 2004.
- [12] M. A. L. Nicolelis, "Actions from thoughts," in *Nature*, vol. 409, 2001, pp. 403-407.
- [13] M. A. L. Nicolelis and J. K. Chapin, "Controlling robots with the mind," *Scientific American*, vol. 287, 2002, pp. 46-53.
- [14] C. G. Gross, C. E. Rocha-Miranda, and D. B. Bender, "Visual properties of neurons in inferotemporal cortex of the Macaque," *J Neurophysiol*, vol. 35, pp. 96-111, 1972.
- [15] C. S. Herrmann, "Human EEG responses to 1-100 Hz flicker: resonance phenomena in visual cortex and their potential correlation to cognitive phenomena," *Exp Brain Res*, vol. 137, pp. 345-353, 2001.
- [16] D. J. Dijk, D. G. Beersma, and R. H. van den Hoofdakker, "All night spectral analysis of EEG sleep in young adult and middle-aged male subjects," *Neurobiol Aging*, vol. 10, pp. 677-682, 1989.
- [17] E. V. Evarts, "Activity of neurons in visual cortex of the cat during sleep with low voltage fast eeg activity," *J. Neurophys.*, vol. 25, pp. 812-816, 1962.
- [18] S. Ogawa, T. Lee, A. Kay, and D. Tank, "Brain magnetic resonance imaging with contrast dependent on blood oxygenation," *Proc Natl Acad Sci U S A*, vol. 87, pp. 9868-9872, 1990.
- [19] N. K. Logothetis, "The underpinnings of the BOLD functional magnetic resonance imaging signal," *J Neurosci*, vol. 23, pp. 3963-3971, 2003.
- [20] M. E. Raichle, "Functional brain imaging and human brain function," *J Neurosci*, vol. 23, pp. 3959-3962, 2003.
- [21] J. D. Greene, R. B. Sommerville, L. E. Nystrom, J. M. Darley, and J. D. Cohen, "An fMRI investigation of emotional engagement in moral judgment," *Science*, vol. 293, pp. 2105-2108, 2001.
- [22] K. L. Phan, T. Wager, S. F. Taylor, and I. Liberzon, "Functional neuroanatomy of emotion: A meta-analysis of emotion activation studies in PET and FMRI," *Neuroimage*, vol. 16, pp. 331-348, 2002.
- [23] R. M. Birn, P. A. Bandettini, R. W. Cox, and R. Shaker, "Event-related fMRI of tasks involving brief motion," *Interscience*, vol. 7, pp. 106-114, 1999.

- [24] A. D. Friederici, M. Meyer, and D. Y. von Cramon, "Auditory language comprehension: An event-related fMRI study on the processing of syntactic and lexical information," *Brain and Language*, vol. 74, pp. 289-300, 2000.
- [25] *Microelectrode Array (MEA) User Manual*. Reutlingen, Germany: Multichannel Systems MCS GmbH, 2005.
- [26] S. Chawla, P. Vanhoutte, F. J. Arnold, C. L. Huang, and H. Bading, "Neuronal activity-dependent nucleocytoplasmic shuttling of HDAC4 and HDAC5," *J Neurochem*, vol. 85, pp. 151-159, 2003.
- [27] M. A. Corner, J. van Pelt, P. S. Wolters, R. E. Baker, and R. H. Nuytinck, "Physiological effects of sustained blockade of excitatory synaptic transmission on spontaneously active developing neuronal networks--an inquiry into the reciprocal linkage between intrinsic biorhythms and neuroplasticity in early ontogeny," *Neurosci Biobehav Rev*, vol. 26, pp. 127-85, 2002.
- [28] F. Hofmann, "Functional re-establishment of the perforant pathway in organotypic co-cultures on microelectrode arrays," *Brain Res*, vol. 1017, pp. 184-196, 2004.
- [29] F. H. Arnold, F. Hofmann, P. Bengtson, M. Wittmann, P. Vanhoutte, and H. Bading, "Microelectrode array recordings of cultured hippocampal networks reveal a simple model for transcription and protein synthesis-dependent plasticity," *J Physiol*, vol. 564, pp. 3-19, 2005.
- [30] F. Lante, M. C. de Jesus Ferreira, J. Guiramand, M. Recasens, and M. Vignes, "Low-frequency stimulation induces a new form of LTP, metabotropic glutamate (mGlu(5)) receptor- and PKA-dependent, in the CA1 area of the rat hippocampus," *Hippocampus*, 2005.
- [31] M. J. Berry, J. L. Puchalla, E. Schneidman, and R. A. Harris, "Redundancy in the population code of the retina," *Neuron*, vol. 46, pp. 493-504, 2005.
- [32] A. H. Chen, Y. Zhou, H. Q. Gong, and P. J. Liang, "Luminance adaptation increased the contrast sensitivity of retinal ganglion cells," *Neuroreport*, vol. 16, pp. 371-375, 2005.
- [33] D. J. Bakkum, Shkolnik, A. C., Ben-Ary, G., Gamblen, P., DeMarse, T. B. and Potter, S. M., "Removing some 'A' from AI: embodied cultured networks. Embodied artificial intelligence," *Embodied Artificial Intelligence*, F. Iida, Steels, L. and Pfeifer, R., Ed.: Springer-Verlag, In Press.
- [34] T. B. DeMarse, D. A. Wagenaar, A. W. Blau, and S. M. Potter, "The neurally controlled animat: Biological brains acting with simulated bodies," *Autonom Robots*, vol. 11, pp. 305-310, 2001.

- [35] K. Banach, M. D. Halbach, P. Hu, J. Hescheler, and U. Egert, "Development of electrical activity in cardiac myocyte aggregates derived from mouse embryonic stem cells," *Am J Physiol Heart Circ Physiol*, vol. 284, pp. H2114-23, 2003.
- [36] J. Hescheler, Y. Duan, M. Tang, and H. Linag, "Investigation on spontaneous electrical activity of murine embryonic heart using microelectrode arrays," *Acta Physiologica Sinica*, vol. 58, pp. 65-70, 2006.
- [37] J. Malmivuo and R. Plonsey, *Bioelectromagnetism - Principles and Applications of Bioelectric and Biomagnetic Fields*. New York, NY: Oxford University Press, 1995.
- [38] A. Adler, R. Amyot, R. Guardo, J. H. T. Bates, and Y. Berthiaume, "Monitoring changes in lung air and liquid volumes with electrical impedance tomography," *J Appl Physiol*, vol. 83, pp. 1762-1767, 1997.
- [39] I. Frerichs, J. Hinz, P. Herrmann, G. Weisser, G. Hahn, T. Dudykevych, M. Quintel, and G. Hellige, "Detection of local lung air content by electrical impedance tomography compared with electron beam CT," *J Appl Physiol*, vol. 93, pp. 660-666, 2002.
- [40] V. Cherepenin, "A 3D electrical impedance tomography (EIT) system for breast cancer detection," *Physiol Meas*, vol. 22, pp. 9-18, 2001.
- [41] Y. Zou and Z. Guo, "A review of electrical impedance techniques for breast cancer detection," *Med Eng Phys.*, vol. 25, pp. 79-90, 2003.
- [42] J. Keener and J. Sneyd, *Mathematical Physiology*. New York, NY: Springer-Verlag, 1998.
- [43] K. S. Cole and H. J. Curtis, "Electric impedance of the squid giant axon during activity," *The Journal of General Physiology*, vol. 22, pp. 649-670, 1939.
- [44] A. L. Hodgkin and A. F. Huxley, "Currents carried by sodium and potassium ions through the membrane of the giant axon of *Loligo*," *J Physiol*, vol. 116, pp. 449-472, 1952.
- [45] A. L. Hodgkin and A. F. Huxley, "Measurement of current-voltage relations in the membrane of the giant axon of *Loligo*," *J Physiol*, vol. 116, pp. 424-448, 1952.
- [46] A. L. Hodgkin and A. F. Huxley, "A quantitative description of ion currents and its applications to conduction and excitation in nerve," *J Physiol*, vol. 116, pp. 500-544, 1952.
- [47] A. L. Hodgkin and A. F. Huxley, "The components of membrane conductance in the giant axon of *Loligo*," *J Physiol*, vol. 116, pp. 473-496, 1952.

- [48] A. L. Hodgkin and A. F. Huxley, "The dual effect of membrane potential on sodium conductance in the giant axon of *Loligo*," *J Physiol*, vol. 116, pp. 497-506, 1952.
- [49] K. Boone, D. Barber, and B. Brown, "Imaging with electricity: report of the European Concerted Action on Impedance Tomography," *J. Med Eng Technol*, vol. 21, pp. 201-32, 1997.
- [50] G. Grimnes and O. G. Martinsen, *Bioimpedance and Bioelectricity Basics*. London, UK: Academic Press, 2000.
- [51] D. Holder, ed., *Clinical and Physiological Applications of Electrical Impedance Tomography*. London, UK: UCL Press, 1993.
- [52] D. Holder, *Electrical Impedance Tomography of Brain Function*. London, UK: IOP Publishing, 2005.
- [53] J. G. Webster, ed., *Electrical Impedance Tomography*. Bristol, UK: Adam Hilgar, 1990.
- [54] W. R. Adey, R. T. Kado, and J. Didio, "Impedance measurements in brain tissue of animals using microvolt signals," *Experimental Neurology*, vol. 5, pp. 47-66, 1962.
- [55] A. Van Harreveld and J. P. Schade, "Changes in the electrical conductivity of cerebral cortex during seizure activity," *Experimental Neurology*, vol. 5, pp. 383-400, 1962.
- [56] N. A. Aladjolova, "Slow electrical processes in the brain," *Progress In Brain Research*, vol. 7, pp. 155-237, 1964.
- [57] J. B. Ranck, Jr., "Specific impedance of rabbit cerebral cortex," *Experimental Neurology*, vol. 7, pp. 144-52, 1963.
- [58] S. E. Fox, "Membrane potential and impedance changes in hippocampal pyramidal cells during theta rhythm," *Experimental Brain Research*, vol. 77, pp. 283-294, 1989.
- [59] S. E. Fox and C. Y. Chan, "Location of membrane conductance changes by analysis of the input impedance of neurons. II. Implementation," *Journal of Neurophysiology*, vol. 54, pp. 1594-1606, 1985.
- [60] L. Geddes and L. E. Baker, "The specific resistance of biological material-a compendium of data for the biomedical engineer and physiologist," *Med Biol Eng*, vol. 5, pp. 271-93, 1967.
- [61] A. T. Tidswell, A. Gibson, R. H. Bayford, and D. S. Holder, "Electrical impedance tomography of human brain activity with a two-dimensional ring of scalp electrodes," *Physiol Meas*, vol. 22, pp. 167-75, 2001.

- [62] K. A. Klivington and R. Galambos, "Rapid resistance shifts in cat cortex during click-evoked responses," *Journal of Neurophysiology*, vol. 31, pp. 565-573, 1968.
- [63] W. T. Frazier, E. R. Kandel, I. Kupfermann, R. Waziri, and R. E. Coggeshall, "Morphological and functional properties of identified neurons in the abdominal ganglion of *Aplysia californica*," *Journal of Neurophysiology*, vol. 30, 1967.
- [64] J. L. Novak and B. C. Wheeler, "Recording from the *Aplysia* abdominal ganglion with a planar microelectrode array," *IEEE Transactions on Biomedical Engineering*, vol. BME-33, pp. 196-202, 1986.
- [65] S. Haykin, *Adaptive Filter Theory (4th Edition)*. Upper Saddle River, NJ: Prentice Hall, 2002.
- [66] R. J. Sadleir, S. C. Grant, X. Silver, S. U. Zhang, E. J. Woo, S. Y. Lee, T. S. Kim, S. H. Oh, B. I. Lee, and J. K. Seo, "Magnetic resonance electrical impedance tomography (MREIT) at 11 tesla field strength: preliminary experimental study," presented at Proc. 5th BEM and 5th NFSI, Minneapolis, Minnesota, 2005.

BIOGRAPHICAL SKETCH

Hany Elmariah was born on August 10, 1982 in St. Petersburg, Florida. Two years later, his family relocated to Panama City, Florida where he spent the rest of his childhood. Hany attended Bay High School, where he fostered strong interests in Biology and Physics. As an undergraduate at Duke University, Hany earned a Bachelor of Science in Physics, while also completing the prerequisites to pursue a graduate education in the health sciences. This background proved useful for his next academic pursuit, a Master of Science in Biomedical Engineering at the University of Florida. Hany plans to attend medical school in the fall of 2007.